Impact of Josephson Junction Array modes on Fluxonium Readout

Shraddha Singh[1, 2, 3, *] Gil Refael,[3, 4] Aashish Clerk,[5, 3] and Emma Rosenfeld[3, †]

[1]*Department of Applied Physics and Physics, Yale University, New Haven, Connecticut 06511, USA*
[2]*Yale Quantum Institute, Yale University, New Haven, Connecticut 06511, USA*
[3]*AWS Center for Quantum Computing, Pasadena, CA 91125, USA*
[4]*Institute for Quantum Information and Matter,*
California Institute of Technology, Pasadena, CA 91125
[5]*Pritzker School of Molecular Engineering, University of Chicago, Chicago, Illinois 60637, USA*
(Dated: October 2, 2024)

Fluxonium qubits, known for their high coherence and fast gates, are a promising candidate for superconducting architectures. High-fidelity measurement of these qubits is a crucial component in employing a fluxonium-based architecture for fault-tolerant quantum computing. We present an analysis of dispersive readout in fluxonium qubits, specifically considering the 'parasitic' internal modes of a Josephson junction array (JJA) which constitutes the inductive shunt in the circuit. Measurement of superconducting circuits is currently limited by state transitions in the qubit, when increasing photons in the readout mode, also known as measurement-induced state transitions (MIST). Our analysis reveals that coupling to the parasitic modes of JJA introduces additional state transitions during fluxonium readout. Consequently, such parasitic-mode-assisted MIST processes, which we refer to as p-MIST, can lower the onset of MIST processes to as low as ~ 10 average photons in the readout mode, severely impacting the readout performance. We verify that, even upon neglecting nonlinearities in the JJA, a significant number of these parasitic transitions, mediated by the coupling of the parasitic mode to the qubit mode, occur at considerable rates. The residual population in the parasitic modes from p-MIST also causes significant dephasing of the resetted fluxonium qubit, after the readout pulse, limiting the performance of the qubit for future use. We extend our findings across various fluxonium circuits, analyzing the dependency of qubit-parasitic mode coupling on different circuit parameters. Our results underscore the substantial impact parasitic modes can have on the readout fidelity, even upon neglecting any nonlinearities, and the coherence of highly anharmonic superconducting circuits.

I. INTRODUCTION

The fluxonium circuit, a Josephson junction shunted by an inductor and a capacitor, is a promising qubit due to its large anharmonicity, flexible parameters, and long lifetimes [1–4]. Recent high-fidelity single- [5] and two-qubit [6, 7] gate demonstrations show error probabilities of $\sim 10^{-4}$ and $\sim 10^{-3}$, respectively, which likely can be improved further [8–12]. For this work, we assume that the inductive shunt in a fluxonium circuit constitutes a Josephson junction array (JJA) [13, 14] due to its relatively low loss, large inductance, and small capacitance. The internal modes of the fluxonium circuit identify a qubit mode where the computational states reside, and several additional "parasitic" modes, from the charge islands in the junction array [15].

Typically, fluxonium qubit measurements are performed by dispersively coupling the circuit to a readout mode [5]. Dispersive readout, commonly used for its fast, single-shot capabilities, offers large signal-to-noise ratios and is expected to be quantum non demolition (QND) [16]. However, the fidelity and speed of this readout strategy has been limited by spurious transitions of the computational states to higher energy states [17–22], often called Measurement-Induced State Transitions (MIST). Unlike the weakly anharmonic transmon, a fluxonium circuit is highly nonlinear [3], which increases the likelihood of MIST processes [23]. Additionally, any spurious modes, such as

the JJA modes mentioned previously, box modes from chip packaging, or slot line modes in the chip geometry, may also play a role in MIST, as shown in Fig. 1. However, a detailed analysis of MIST in the presence of such spurious modes during dispersive readout of a superconducting qubit is still pending.

In this work, we analyze the state transitions during the dispersive readout of a fluxonium circuit, especially focusing on the effects that arise due to the parasitic modes of the JJA-fluxonium. Fig. 2 shows our measurement circuit for a heavy fluxonium circuit at the flux sweet spot ($\varphi_{ext} = 0.5\Phi_0$), an experimentally-relevant choice for maximizing qubit coherence [2, 5, 24, 25]; however, parasitic effects in the case of several circuit modifications are also discussed. While this figure shows a parallel circuit connection we have also analyzed different grounding configurations for single-point connection circuits in App. A. In the main text, we mainly discuss the parallel circuit in Fig. 2 with circuit parameters inspired by the experiment in Ref. [5]. We analyze the population in the first three eigenstates in the qubit mode, to include experiments with a heavy fluxonium that use the first two levels (01) for computation and the second two levels (12) for measurement [5]. With our Hamiltonian derivations inspired from [26], we find that the coupling strength between the qubit mode and the parasitic modes can be ~ 100 MHz, approximately ten-fold higher than the qubit-readout coupling strength.

Treating the readout mode classically [20, 21], we perform a Floquet simulation of this system and identify predominant MIST processes, shown in Fig. 3. In particular, our simulation of the dispersive readout

N	φ_{ext}	E_{J_p}	E_{C_p}	E_C	E_{C_j}	E_{J_j}	$E_{C_{g,j}}$	$E_{C_{g,p}}$	E_c
122	$0.5\Phi_0$	7.30	0.74	1.34	0.74	60	194	1.94	19.40

TABLE I. Circuit parameters for Fig. 2(a) inspired by [5]. All energies are given in GHz. Here $\Phi_0 = h/2e$ denotes the magnetic flux quantum. The capacitive energies $E_{C'} = \frac{19.4}{C'(fF)}$ GHz are computed from the corresponding capacitances C'. See Table V in App. B for the values of capacitances.
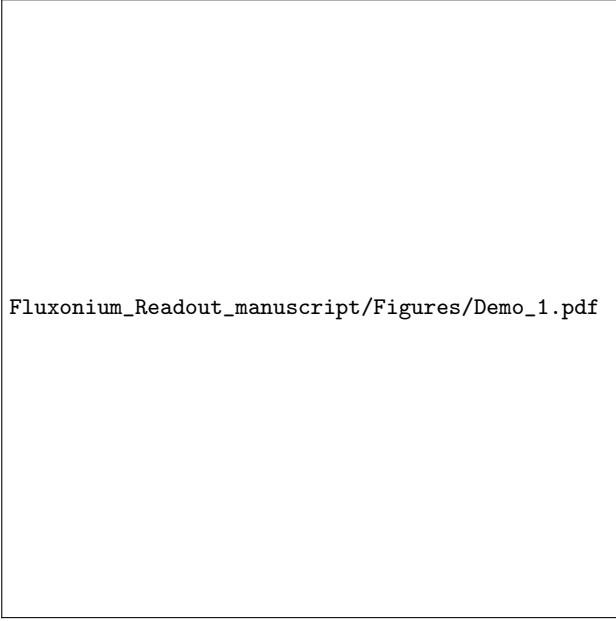
FIG. 1. Schematic of qubit state transitions driven by a readout oscillator (R) with parasitic modes from a Josephson junction array (JJA). The abstract circuit diagram is paired with energy profiles, showing energy in a coherent state of the driven readout mode (black) splitting into JJA parasitic modes (red), leaving enough energy for excitation in the qubit mode (blue).
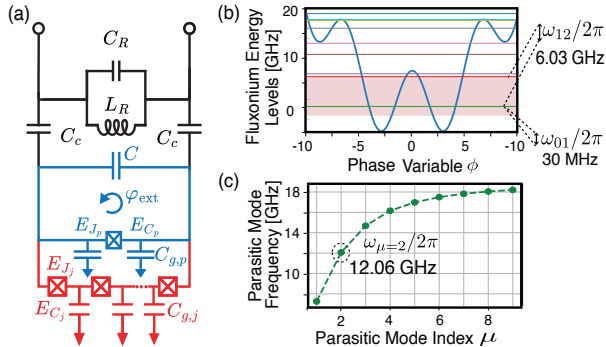

FIG. 2. (a) Fluxonium readout circuit. The color scheme shows primary components that correspond to various modes, shown in Fig. 1, when a JJA fluxonium circuit is connected to a readout resonator (R). The subscripts p, j denote components of the phase-slip junction and the JJA, respectively. This circuit shows coupling capacitances (C_c), readout frequency parameters ($\omega_r/2\pi = 1/\sqrt{L_R C_R}$), parasitic ground capacitances in JJA ($C_{g,j}$) and next to the phase-slip junction ($C_{g,p}$). The differential capacitance C adjusts the charging energy of the qubit mode (see Table II). (b) Fluxonium mode energy levels in units of h, with the highlighted area showing the first three levels essential for certain readout schemes [5]. (c) Parasitic mode frequencies ω_μ. The lowest even mode $\mu = 2$ has the strongest coupling to the qubit (see Fig. 13).

process identifies state transitions of the fluxonium mode under dispersive readout, which occur only in the presence of the coupling between the qubit mode and the parasitic mode. We term these phenomena Parasitic-Mode-Induced State Transition (p-MIST). At particular readout resonator frequencies, we find that the onset of p-MIST can occur with only ~ 10 photons in the readout resonator, well within the desired power for high signal-to-noise ratios in dispersive readout [27].

Our work identifies transition pathways not seen in previous Transmon-based MIST analyses, which occur because of the highly nonlinear nature of the fluxonium spectrum and the presence of strongly coupled parasitic modes. To understand the Floquet simulation results, we identify the processes that cause these transitions in Table III using energy-conservation processes which are supported by a perturbative estimation from Fermi's Golden (FG) rule calculations. We provide information on the analytically calculated stark-shifted eigenenergies and FG rates of each transition in App. C 3. The total number of MIST processes increases by 50% in the presence of the parasitic mode that couples the strongest to the qubit mode. Examples of some interesting MIST processes are as follows. A higher energy fluxonium state ($|2\rangle$) may exchange population with a lower energy state ($|0\rangle$), through excitation exchange with the readout resonator in the presence of a parasitic mode. In our simulations, we also observe transitions between parity-conserving states which are impossible via a first-order process for $\varphi_{ext} = 0.5\Phi_0$. We also observe that two higher fluxonium states are hybridized into an equal superposition state when the drive frequency is resonant with their transition frequency; such hybridization allows for increased p-MIST processes.

We compute the rates of all p-MIST processes involving the $|1\rangle$ state, which is used for both measurement and computation, to justify that these transitions can be significant. The rates are computed independently from, (1) the Hamiltonian dynamics of the system, and (2) the quasi-energy gap obtained via the Floquet simulations in Landau-Zener probability calculations. We ringed up the drive towards the steady-state readout mode occupation of $\bar{n}_r = 50$ to mimic dissipation in the readout resonator [20, 21]. Both methods indicate in perfect agreement that the p-MIST processes observed can be significant at a ring-up rate of $\kappa_r = 1$ MHz. These calculations show that p-MIST processes with a quasienergy gap of ~ 0.5 MHz at the avoided crossings occur with significant probability. The avoided crossings of such strong transitions can be correctly predicted using first-order perturbative calculations. However, the two methods do not agree for $\kappa_r \geq 10$, indicating that the two-level Landau Zener physics does not capture the evolution of highly anharmonic fluxonium circuits.

Additionally, we show that the residual p-MIST population in the parasitic modes, which remains *af-*

ter a readout pulse, begets significant dephasing of the qubit mode. Since these parasitic modes are long-lived [13] and strongly coupled to the qubit mode, such residual population must be treated with care when designing the circuit. We numerically show that the dephasing error probability due to excited parasitic modes with finite internal quality factor is above the surface code error correction threshold for parameters used in the current experimental setups [5, 13, 25]. This effect indicates that, without proper care, the dephasing due to p-MIST could limit the performance of a fluxonium architecture.

Finally, we generalize our results to several circuit modifications by analyzing the sensitivity of the parasitic mode-qubit coupling strength for different readout frequencies, parasitic mode frequencies, qubit mode frequencies, ground capacitances, and number of junctions in the array. First, we show that these effects are mediated strictly by the coupling between the qubit mode and the parasitic mode. We also explore lower readout frequencies in Fig. 9 and show that increased p-MIST processes can be introduced if the parasitic frequency is an integer multiple of the drive frequency. In addition, we simulated a ~ 300 MHz circuit with larger parasitic mode frequencies, inspired by the experiment in Ref. [6]. We find that for comparable frequencies and coupling strengths, this circuit shows a much lower number of MIST processes, an observation that needs further investigation beyond the scope of this work. However, even in this case, half the number of transitions (one out of two) are p-MIST for similar coupling strengths. While our analysis does not demonstrate an exhaustive study over the entire parameter space, it shows that the parasitic modes of a junction array introduce additional constraints on the circuit design of high-coherence fluxonium qubits.

The article is structured as follows: Sec. II details the readout circuit and its strong parasitic coupling under a linear JJA approximation. Through this assumption, our work presents the lower bound on the effects of JJA parasitic modes on the readout of a fluxonium circuit. Sec. III covers readout dynamics, including MIST processes and dephasing from parasitic modes. Sec. IV analyzes the effects of coupling strengths on p-MIST, and investigates different ranges of readout frequencies and parasitic mode frequencies using an energy-conservation picture. Finally, in Sec. V we discuss directions for future work towards our analysis.

II. FLUXONIUM READOUT CIRCUIT

We consider a JJA-fluxonium circuit dispersively coupled to a readout mode as shown in Fig. 2. The parameters for circuit design used in our work, listed in Table I, are motivated by recent experiments [5, 7]. We focus on the fluxonium circuit at the "sweet spot" for maximal qubit coherence times. This choice is also expected to reduce the number of allowed transitions in the circuit, as transitions between parity-conserving states via first-order processes are forbidden in this case. Here, the qubit frequency ($\omega_{01}/2\pi$) is ~ 30

MHz and the plasmon frequency ($\omega_{12}/2\pi$) is ~ 6 GHz, in this "heavy" fluxonium regime (see Table II for a full list of readout parameters). The dispersive shift on the qubit computational states due to the readout resonator is not sufficiently strong for high signal-to-noise, at $\chi_{01} \sim 0.2$ MHz; in practice, higher excited states of the fluxonium qubit mode may be populated intentionally for improved readout fidelity [5]. Thus, to also capture effects from measurement schemes that use higher levels $(1, 2)$, we consider the population in the lowest three states of the qubit mode.

Our work specifically investigates the role of the JJA, which comprises the inductive shunt of the fluxonium. The array comprises $N + 1$ junctions and N ground capacitances due to the JJA (C_{g_n}) [25]. We assume an ordered array with identical junctions and parasitic ground capacitances between these junctions ($C_{g_1} = .. = C_{g_{N-1}} = C_{g,j}$). Two additional identical ground capacitances near the phase-slip junctions may have different values, with $C_{g_0} = C_{g_N} = C_{g,p} \neq C_{g,j}$. The JJA fluxonium circuit has N internal degrees of freedom [15, 26]: one qubit mode (ϕ) and $N - 1$ parasitic modes (μ), where μ ranges between $1, ..., N - 1$. These modes are coupled via the ground capacitances. In our notation, we label the readout mode as r. The qubit charge and flux quadratures are denoted by $\hat{N}_\phi$ and $\hat{\phi}$ where $[\hat{\phi}, \hat{N}_\phi] = \frac{i\hbar}{2}$. We denote the photon loss and gain operators using $\hat{a}_r, \hat{a}_\mu$ and $\hat{a}_r^\dagger, \hat{a}_\mu^\dagger$, respectively. We simplify the problem by treating all but the qubit mode as harmonic oscillators as assumed in previous works [15, 21, 26]. This assumption will lower bound the effects of JJA parasitic modes on qubit performance for driven fluxonium circuits. In units of $\hbar = 1$, the Hamiltonian of an undriven fluxonium measurement circuit has the form (see App. A for derivation)

$$\hat{H} = \hat{H}_\phi + \hat{H}_\mu + \hat{H}_r + \hat{H}_{int}, \tag{1}$$

where the qubit Hamiltonian $\hat{H}_\phi$ (with JJA inductive energy $E_L = E_{J_j}/N$) is

$$\hat{H}_\phi/2\pi = 4\tilde{E}_c^\phi \hat{N}_\phi^2 + E_{J_p} \cos\hat{\phi} + E_L \hat{\phi}^2/2, \tag{2}$$

the junction array and readout Hamiltonians are $\hat{H}_\mu = \sum_\mu \omega_\mu \hat{a}_\mu^\dagger \hat{a}_\mu$ and $\hat{H}_r = \omega_r \hat{a}_r^\dagger \hat{a}_r$, respectively. The qubit charging energy deviates from the target value of $E_c^\phi = 1$ GHz due to parasitic capacitance. The coupling between the three modes is described by the interaction Hamiltonian

$$\hat{H}_{int} = g_{\phi r} \frac{\hat{N}_\phi}{N_{\phi,ZPF}} (\hat{a}_r - \hat{a}_r^\dagger)$$
$$- \sum_\mu g_{\phi\mu} \frac{\hat{N}_\phi}{N_{\phi,ZPF}} (\hat{a}_\mu - \hat{a}_\mu^\dagger)$$
$$- \sum_\mu g_{\mu r} (\hat{a}_r - \hat{a}_r^\dagger)(\hat{a}_\mu - \hat{a}_\mu^\dagger). \tag{3}$$

where the zero-point fluctuation value is $N_{\phi,ZPF} = 1.4$. All Hamiltonian variables in this Hamiltonian are given in Table. II.

Qubit (ϕ) & Readout (r) Parameters	$\omega_{01}/2\pi$	$\omega_{12}/2\pi$	$\tilde{E}_c^\phi$	$g_{\phi r}/2\pi$	$\chi_{\phi r}(01)/2\pi$	$\chi_{\phi r}(12)/2\pi$	$\omega_r/2\pi$	$\kappa_r/2\pi$
	30 MHz	6.04 GHz	0.92 GHz	25.50 MHz	0.18 MHz	0.98 MHz	8.50 GHz	1 MHz
Parasitic-Mode ($\mu=2$) Parameters			$g_{\phi\mu}/2\pi$	$g_{\mu r}/2\pi$	$\chi_{\phi\mu}(01)/2\pi$	$\chi_{\phi\mu}(12)/2\pi$	$\omega_\mu/2\pi$	Q_μ
			157 MHz	4.22 MHz	−1.10 MHz	5 MHz	12.06 GHz	10^4

TABLE II. Parameters for qubit mode ϕ, readout mode r and closest even parasitic mode $\mu = 2$. All quantities are derived and computed analytically using circuit parameters listed in Table. I (see App. B for details). **Qubit-Readout Parameters:** (ω_{ij}) qubit $i \rightarrow j$ splitting frequency; ($\tilde{E}_c^\phi$) qubit charging energy; ($g_{\phi r}$) qubit-readout coupling; ($\chi_{\phi r}(ij)$) dispersive shift due to readout mode in the two-level ij system; (ω_r) readout mode frequency; (κ_r) decay rate of the readout resonator. **Parasitic-Mode Parameters:** ($g_{\phi\mu}$) qubit-parasitic coupling; ($g_{\mu r}$) parasitic-readout coupling; ($\chi_{\phi\mu}(ij)$) dispersive shift due to parasitic modes in the two-level ij system; (ω_μ) mode frequency; and (Q_μ) internal quality factor inspired by [13].

Our coupling strengths follow the same relative behaviour as observed in Ref. [26], but with a different set of parameters as chosen here. We find that the lowest-frequency even parasitic mode $\mu = 2$ has the strongest coupling to the qubit mode (see Fig. 13 in App. B); parasitic parameters are quoted in Table I. Ref. [26] shows that the symmetry of the parallel circuit in Fig. 2 prevents coupling between odd parasitic modes (including $\mu = 1$) and other circuit modes. We extend this result to two additional circuits, with different ground circuit configurations, showing qualitatively consistent conclusions across all in App. A. The circuits yield the same Hamiltonian when the differential capacitance C and couling capacitance C_c are altered such that qubit frequency and qubit-readout coupling are same across all three circuits (see Table IV in App. A). With these observations, in the rest of this work, we will use the parallel circuit from Fig.2 using parameters given by Tables I, II in Eq. 1 with only the qubit (ϕ), the strongest coupled parasitic mode ($\mu = 2$) and the readout resonator (r). For details on other parasitic modes and their circuit parameters, see Apps. B.

As reported in Table I, the qubit couples roughly six times more strongly to the parasitic mode at $\mu = 2$ than it does to the readout r [28]. As we highlight in the next section, such strong couplings can lead to measurement-induced state transitions assisted by parasitic modes, termed "p-MIST". This strong coupling also indirectly couples the readout with the parasitic modes, through the qubit mode with strength $g_{\mu r} \propto g_{\phi\mu}$.

III. PARASITIC-MODE-ASSISTED MIST: P-MIST

In this section, we will analyze how the presence of a parasitic mode ($\mu = 2$) affects the dynamics of a driven fluxonium circuit in a readout context. To simulate the linear drive on the readout resonator, we add a drive term $V_d = i\xi(\hat{a}_r - \hat{a}_r^\dagger)\cos\omega_d t$ to the system Hamiltonian in Eq. 1. If we consider the fluxonium qubit mode, parasitic modes, and readout resonator, numerical analyses of several excitations in the circuit would require a prohibitively large Hilbert space. For example, the highly nonlinear nature of the fluxonium qubit spectrum results in a minimum Hilbert

space dimension of at least ~ 20 for an accuracy of 1 MHz, while we expect to drive many photons in the readout cavity. To truncate our Hilbert space to feasible dimensions for numerical simulations, here we only include a single parasitic mode $\mu = 2$ (as previously justified in Sec. II), and we replace the readout mode with a classical drive term [18, 20, 21] using the derivation in App. C. Under this semi-classical approximation, we give the driven circuit Hamiltonian with only two modes, ϕ and $\mu = 2$

$$\hat{H}_{s.c.}(\bar{n}_r) = \hat{H}_0 + \hat{V}_{s.c.}(\bar{n}_r) \qquad (4)$$

which includes the parent or bare Hamiltonian,

$$H_0 = \hat{H}_\phi + \hat{H}_\mu - \frac{g_{\phi\mu}}{N_{\phi,ZPF}}\hat{N}_\phi(\hat{a}_\mu - \hat{a}_\mu^\dagger) \qquad (5)$$

and the modified drive term $V_{s.c.}$,

$$\hat{V}_{\text{s.c.}}(\bar{n}_r) = \frac{\xi_{\phi r}(\bar{n}_r)}{N_{ZPF,\phi}}\hat{N}_\phi \cos\omega_d t + \xi_{\mu r}(\bar{n}_r)\hat{N}_\mu \cos\omega_d t, \qquad (6)$$

where $\xi_{\mu(\phi)r}(\bar{n}_r) = 2g_{\mu(\phi)r}\sqrt{\bar{n}_r}$, and $\bar{n}_r$ denotes average readout photons, respectively. We shall call the quantities $\xi_{\phi r/\mu r}$ qubit and parasitic drive strengths, respectively. Note that a similar semi-classical approximation could have been carried out to remove the parasitic mode from the picture, however, the quantum fluctuations cannot be ignored in this case since the parasitic modes are not expected to be highly populated in readout experiments, and also, doing this will not capture the physics we are interested in.

Our primary task is to analyze p-MIST processes which introduce simultaneous transitions in the parasitic mode and the qubit mode. To identify the state transitions in the driven circuit, we first examine the eigenspace of the bare Hamiltonian H_0 in Eq. 5. Commonly, for the analysis of a fluxonium circuit, the basis $|k\rangle_\phi \otimes |n\rangle_\mu$ is used, where the parasitic mode μ is mostly ignored [23]. We label the hybridized eigenstates of H_0 as $|\tilde{k}, \tilde{n}\rangle$ to indicate the states, it has maximum overlap with, in the disjoint Hilbert space $|k\rangle_\phi \otimes |n\rangle_\mu$. This labeling will help us better understand the effects of p-MIST on the qubit subspace.

Next, we perform a Floquet simulation of the driven circuit to identify the state transitions in the system. We simulate the system dynamics for a range of readout resonator frequencies, ω_d, and ring up the various drive strengths $\xi_{\mu/\phi}$ to emulate the addition of

photons in the readout resonator. We find that the presence of the parasitic mode $\mu = 2$ significantly increases the number of MIST processes in the system. We analyze the processes that cause these transitions and quantify their rates using perturbative approaches and Landau Zener probability calculations [29]. We also show that the residual population in the parasitic modes, after a readout pulse, can lead to significant dephasing of the resetted qubit mode, limiting the performance of the qubit for any future use.

A. Floquet Simulations
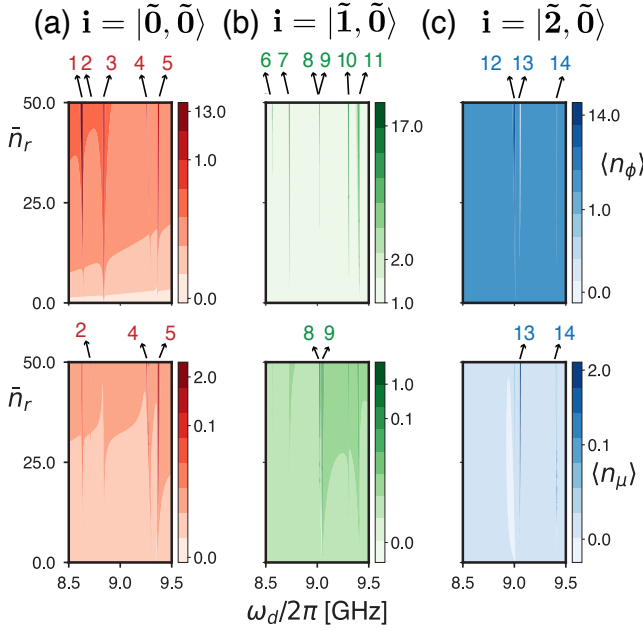
FIG. 3. p-MIST processes in Floquet Simulations. Columns show results for branch analysis starting in the dressed hybridized eigenstate $i = |\tilde{k}, \tilde{0}\rangle$, with maximum overlap to the un-hybridized states $|k\rangle_\phi \otimes |0\rangle_{\mu=2}$. **Top row:** Average fluxonium excitation $\langle n_\phi \rangle$. **Bottom row:** Average excitation of the first-even parasitic mode $\mu = 2$ $\langle n_\mu \rangle$. The plots are shown in log scale as a visual aid for all marked transitions, explicitly listed in Table III. See Figs. 17-19 of App. C 3 for quasienergies.

Our first numerical analysis uses Floquet simulation of the Hamiltonian $H_{s.c.}$ (see Eqs. 4) while varying $\bar{n}_r$ as the Floquet parameter, for various drive frequencies ω_d. To reduce the numerical complexity, we only focus on transitions involving the lowest 20 levels in the qubit subspace ϕ and 2 levels in the harmonic oscillator mode $\mu = 2$ with a maximum of 50 photons in the readout resonator. In App. C 1 we discuss the truncation [30] used to obtain our results. As indicated before, we will study transitions from states $|i\rangle = |\tilde{\phi}, \tilde{\mu}\rangle$ where $\phi = \{0, 1, 2\}$ and $\mu = 0$. With $\omega_\mu = 12.06$ GHz, the analysis in this section will consider the regime of negative detuning where, $\omega_{\mu=2} > \omega_d = \omega_r >> \omega_q$, and can be replicated for any other parasitic mode. We also analyze effects of an alternative circuit with $\omega_{\mu=2} \sim 16$ GHz and $\omega_\phi \sim 300$ MHz in Sec. IV.

Inspired by [20, 21], we extract p-MIST processes by tracking a hybridized fluxonium eigenstate in a Floquet simulation while ringing up the drive strengths, a method known as *branch analysis*. Our drive ring-up emulates the addition of a single readout photon by incrementing $\bar{n}_r$ for each tracking step at $t = 0$. The simulation begins in an eigenstate $|i\rangle$ of the bare Hamiltonian $\hat{H}_0$ (see Eq. 5). This eigenstate is the same as the dressed eigenstate of the driven circuit Hamiltonian $H_{s.c.}$ (see Eq. 4) at $\bar{n}_r = 0$, $|i\rangle_{\bar{n}_r=0}$. Next, we compute the dressed eigenstates of the modified Hamiltonian $\hat{H}_{s.c.}$ at $\bar{n}_r = 1$, $\{|m\rangle_{\bar{n}_r=1}\}$, corresponding to a single photon increase in the readout resonator. We then track the eigenstate $|i\rangle_{\bar{n}_r=1}$ in this new eigenspace that has maximum overlap with $|i\rangle_{\bar{n}_r=0}$, identifying it as the new eigenstate associated with the branch of $|i\rangle$. This process is repeated with the increment $\Delta \bar{n}_r = 1$, such that at each tracking step t_k, a new state is chosen from the Floquet eigenspace of the modified Hamiltonian as, yielding the branch

$$|i_{\bar{n}_r=k}\rangle : \max_m |\langle i_{\bar{n}_r=k-1}|m_{\bar{n}_r=k}\rangle|^2. \quad (7)$$

Our method is different from Ref. [20, 21] in that we perform the branch analysis of the modified Hamiltonians $H_{s.c.}(\bar{n}_r)$ at a fixed time $t = 0$ while linearly varying $\bar{n}_r$. In the time evolution picture, the drive powers $|\xi_{\phi r}|^2, |\xi_{\mu r}|^2 \propto \bar{n}_r$ are increasing linearly in time as $\bar{n}_r = \kappa t/T$, where $\kappa \Delta t = T$. For each $|m_{\bar{n}_r=i}\rangle$ tracked in the branch, we compute:

1. the average expectation values of $\hat{n}_\phi = \sum_i i |i_t\rangle \langle i_t|$ where i is the index for the bare fluxonium eigenstates,

2. the expectation value of $\hat{n}_\mu = a^\dagger_{\mu=2} a_{\mu=2}$, i.e., the number operator of the harmonic oscillator defined by the parasitic mode $\mu = 2$, and

3. the quasi-energy spectrum $E_i \mod \omega_d$.

Fig. 3 illustrates our main result, showing p-MIST for initial states that have maximum overlap with states $|0\rangle_\phi$, $|1\rangle_\phi$ and $|2\rangle_\phi$ in the fluxonium subspace and the ground state $|0\rangle_{\mu=2}$ in the parasitic subspace. We focus on readout drive frequencies between $8.5 - 9.5$ GHz [31] while other ranges of readout frequencies are also discussed in Sec. IV. The y-axes of the various plots show average readout photons $\bar{n}_r$ which directly shows the variation in drive power $|\xi_{\phi r}|^2, |\xi_{\mu r}|^2$ used in Eq. 6. We plot the figure in logarithmic scale to make it easier to see transition 2 which would become visible in a linear scale plot only at $\bar{n}_r = 48$. We give the corresponding linear scale plot for comparison with other Floquet figures in the main text, and including quasi-energies, in App. C 3. Any streak or sharp change in color in these figures represents a sudden and significant jump in the respective population, or MIST.

The parasitic transitions or p-MIST correspond to simultaneous jumps in the population of the modes ϕ (Figs. 2a-2c, top row) and $\mu = 2$ (Figs. 2a-2c, bottom row), as $\bar{n}_r$ (or, drive power) varies. At these points, an avoided crossing in the quasi-energies

Transition No. (see Fig. 3)	Fluxonium MIST Process	Threshold Drive Photon	Drive Frequency (ω_d)	Quasienergy Gap (Δ_{ac})	p-MIST	Drive Photons Absorbed (see Fig. 8)
1.	$|\tilde{0},\tilde{0}\rangle \longleftrightarrow |\tilde{13},\tilde{0}\rangle$	13	8.64 GHz	0.90 MHz	×	3
2.	$|\tilde{0},\tilde{0}\rangle \longleftrightarrow |\tilde{4},\tilde{2}\rangle^{*}$	48	8.71 GHz	0.06 MHz	✓	4
3.	$|\tilde{0},\tilde{0}\rangle \longleftrightarrow |\tilde{8},\tilde{0}\rangle$	$\bar{n}_r \to 0$	8.84 GHz	−	×	2
4.	$|\tilde{0},\tilde{0}\rangle \longleftrightarrow |\tilde{6},\tilde{1}\rangle^{*}$	46	9.25 GHz	1.63 MHz	✓	2
5.	$|\tilde{0},\tilde{0}\rangle \longleftrightarrow |\tilde{3},\tilde{1}\rangle$	12	9.36 GHz	0.56 MHz	✓	2
6.	$|\tilde{1},\tilde{0}\rangle \longleftrightarrow |\tilde{17},\tilde{0}\rangle$	32	8.56 GHz	0.25 MHz	×	4
7.	$|\tilde{1},\tilde{0}\rangle \longleftrightarrow |\tilde{7},\tilde{0}\rangle$	4	8.73 GHz	0.74 MHz	×	2
8.	$|\tilde{1},\tilde{0}\rangle \longleftrightarrow |\tilde{12},\tilde{1}\rangle$	19	9.02 GHz	0.12 MHz	✓	4
9.	$|\tilde{1},\tilde{0}\rangle \longleftrightarrow |\tilde{2},\tilde{1}\rangle$	11	9.05 GHz	0.66 MHz	✓	2
10.	$|\tilde{1},\tilde{0}\rangle \longleftrightarrow |\tilde{14},\tilde{0}\rangle$	7	9.31 GHz	0.50 MHz	×	3
11.	$|\tilde{1},\tilde{0}\rangle \longleftrightarrow |\tilde{9},\tilde{0}\rangle$	2	9.41 GHz	1.19 MHz	×	2
12.	$|\tilde{2},\tilde{0}\rangle \longleftrightarrow |\tilde{12},\tilde{0}\rangle$	1	9.00 GHz	0.73 MHz	×	2
13.	$|\tilde{2},\tilde{0}\rangle \longleftrightarrow |\tilde{0},\tilde{2}\rangle$	38	9.06 GHz	0.53 MHz	✓	2
14.	$|\tilde{2},\tilde{0}\rangle \longleftrightarrow |\tilde{5},\tilde{1}\rangle^{*}$	41	9.41 GHz	2.71 MHz	✓	2

TABLE III. Measurement-induced-state-transition (MIST) observed in Fig. 3. Column 1 lists the numbering used to mark the transitions in Fig. 3. Here $|\tilde{i},\tilde{j}\rangle$ indicates the hybridized eigenstates of H_0 (see Eq. 5) which have the maximum overlap with the state $|i\rangle_\phi \otimes |j\rangle_{\mu=2}$ in the disjoint Hilbert space of qubit mode (ϕ) and parasitic mode ($\mu = 2$). Column 2 lists the MIST processes that start at the lowest average readout photon number $\bar{n}_r$ given by column 3. In some cases, we use $\bar{n}_r \to 0$ to indicate that the drive frequency is exactly resonant with the transition frequency. A '*'-marked state indicates hybridization at lower $\bar{n}_r$ due to preceding transitions [a]. Column 4 yields the quasienergy gap at the avoided crossing labeled as Δ_{ac}. Column 5 represents the drive frequency ω_d at which these transitions occur. Column 6 indicates if the process cannot occur without the parasitic mode, denoted as p-MIST. Column 7 indicates the number of drive photons (#) involved in the energy-conserving process, illustrated in Fig. 8. which is responsible for these transitions. We give a comparison of Fermi's golden rule rates and quasienergies for these processes in App. C 3.

[a] $|\tilde{4},\tilde{2}\rangle^{*}$: $|\tilde{4},\tilde{2}\rangle \longleftrightarrow |\tilde{14},\tilde{2}\rangle$ at $\bar{n}_r = 5, \omega_d = 8.71$ GHz with $\Delta_{ac} = 4.0$ MHz absorbs 2 drive photons
$|\tilde{6},\tilde{1}\rangle^{*}$: $|\tilde{6},\tilde{1}\rangle \longleftrightarrow |\tilde{3},\tilde{1}\rangle$ at $\bar{n}_r \to 0, \omega_d = 9.25$ GHz
$|\tilde{5},\tilde{1}\rangle^{*}$: $|\tilde{5},\tilde{1}\rangle \longleftrightarrow |\tilde{17},\tilde{0}\rangle$ at $\bar{n}_r = 14, \omega_d = 9.41$ GHz with $\Delta_{ac} = 4.2$ MHz absorbs 1 drive photon

of the Floquet states confirms the hybridization of the two states involved in the population exchange (see Figs. 17-19 in App. C 3). Additional resonances may occur at alternate drive frequencies not shown in Fig. 3. Table III lists significant transitions observed in our Floquet simulations, and associated processes which cause them, identified through a perturbative analysis (see App. C 3) and energy conservation (shown later Fig. 8). We note that certain MIST processes, p-MIST or not, involve the unexpected transitions at the flux sweet spot [32] between parity-conserving states, due to virtual excitations via non-parity-conserving states.

The non zero qubit-parasitic mode coupling ($g_{\phi\mu}$) is the source of p-MIST processes, covering roughly half the number of transitions listed in Table. III. This aspect is analyzed in Sec. IV. Such transitions will not be captured if parasitic modes are ignored in the Floquet simulations. An interesting instance is 14, where if the parasitic mode was absent the transition $|\tilde{17},0\rangle \leftrightarrow |\tilde{2},0\rangle$ takes place which is a 3 readout photon process, however, in the presence of parasitic mode $\mu = 2$ this process is broken down to be mediated by the hybridized states $|\tilde{5},\tilde{1}\rangle$ via two 1 readout and 2 readout processes. This, therefore, results in the wrong predictions of rates (see Sec. III B) as well as the final state prediction of these transitions. The number of p-MIST processes will increase when other parasitic modes, with coupling comparable to or greater than the qubit-readout coupling ($\mu = 4, 6, 8$), are included in the Floquet simulations. See Fig. 13

for absolute coupling strengths. Thus, ignoring parasitic modes can lead to wrong prediction of MIST free drive frequencies as well as sometimes may contribute wrong post-MIST state knowledge.

In transition 12, we observe downward transitions from a higher fluxonium level ($|2\rangle_\phi$) to a lower fluxonium level ($|0\rangle_\phi$), a process that would not be observed in the absence of parasitic modes, as it indicates emission of transition photons instead of absorption readout photons. This is possible because in the presence of parasitic mode, the state $|\tilde{0},\tilde{2}\rangle$ has a higher energy compared to $|\tilde{2},\tilde{0}\rangle$ such that absorbing two readout photons results in a p-MIST which is closest to a downward state transition in the disjoint fluxonium subspace.

In transitions 3 and 4 we are driving the resonator at the transition frequency of two higher states (not involved in readout or computation) such that the states immediately start to hybridize into an equal superposition of the two states involved. For example, in transition 4, levels $|3\rangle_\phi$ and $|6\rangle_\phi$ start converging to a population of $\langle n_\phi \rangle = 4.5$ in the fluxonium subspace at $\bar{n}_\mu \to 0$ (see Fig. 17 in App. C 3). While this effect is not limited to p-MIST, we highlight the presence of these effects as an accelerator to p-MIST processes since for each transition frequency ω_{ij} in the fluxonium subspace there are several possible transitions $|\tilde{i},\tilde{n}_\mu\rangle \to |\tilde{j},\tilde{n}_\mu\rangle$, for all $\bar{n}_\mu$. A result of this effect is that a 5 readout-photon parasitic process $|\tilde{6},\tilde{1}\rangle \leftrightarrow |\tilde{0},\tilde{0}\rangle$ will now only require 2 readout photons, thus increasing the chances of an avoided crossing with

the state essential for qubit-based computation.

The MIST processes with no jumps in the qubit subspace, also categorized as p-MIST, will only affect the parasitic modes during readout. However, after the qubit is reset post measurement, such an excited parasitic mode can severely dephase the resetted qubit. Our findings reveal that for our specific circuit choice JJA parasitic modes can significantly populate the parasitic modes in the target readout range. Having identified key transitions that cause these effects we will now calculate how detrimental these processes can be towards qubit readout fidelity and coherence. To this end, we will next compute the probability of a specific transition, involving the state $|\tilde{1}, \tilde{0}\rangle$ used for both computation as well as readout, and its outstanding effect on the qubit coherence, post reset.

B. Transition Probability
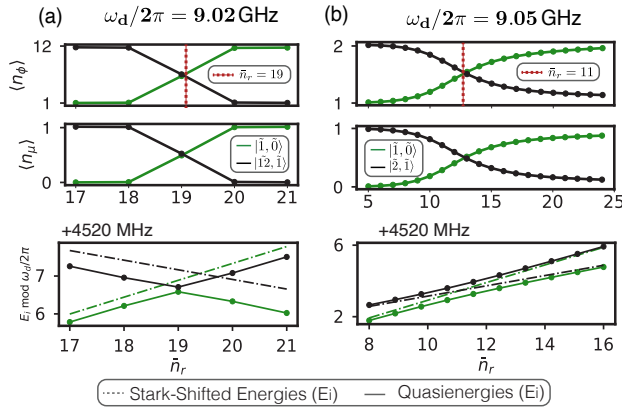
FIG. 4. Examples of p-MIST using transitions **(a)** 8 and **(b)** 9 from Table III involving the $|\tilde{1}, \tilde{0}\rangle$ state, with maximum overlap to the un-hybridized state $|1\rangle_\phi \otimes |0\rangle_{\mu=2}$. **Top row:** Qubit mode average occupation $\langle n_\phi \rangle$. **Middle row:** Parasitic mode average occupation $\langle n_\mu \rangle$. **Bottom row:** Stark-shifted eigen-energies from first-order perturbative calculations (dashed), and quasi-energies (solid) from Floquet simulations showing avoided crossings. Plots are extracted from numerical data used in Fig. 3. The data points are connected by lines for visual aid.

In this section, we estimate the quasienergies and rates of exemplary p-MIST transitions, using the Landau-Zener formalism, respectively. In both the Floquet simulations and Landau-Zener approximations, the spectral gap of an associated transition is a critical figure-of-merit in determining the adiabatic energy exchange probability. Figs. 4(a,b) respectively show the p-MIST explicit population exchange in transitions 8, 9 from Table III involving $|\tilde{1}, \tilde{0}\rangle$, the state involved in computation as well as readout [5]. The simultaneous exchange of population in the qubit mode ϕ, shown in the top panels, and the parasitic mode $\mu = 2$, shown in the middle panels, confirms that the transitions are indeed p-MIST.

The bottom panel of Fig. 4 shows the avoided crossing at the transition point in solid lines. The dashed lines show the eigenenergies calculated in App. C 2 by estimating the Stark shift from the readout drive

onto each state. For small drive amplitudes compared to the gaps in the spectrum, the simple estimate of the eigenenergies using perturbation theory as used in App. C 2 is permissible. This is confirmed by the agreement of the dashed and solid lines in the bottom panel of Fig. 4(b). For this transition, comparing our second-order Fermi's Golden rule estimate (see App. C 3) to the numerically obtained energy gaps in the quasi-energies (solid lines), we find agreement within 1 MHz. The remaining disagreement between the quasi-energies and the estimated eigenenergies suggests that higher-order or non-perturbative corrections become relevant for transitions slower than $\Delta_{ac} = 1$ MHz. Notably, both the transitions shown in Fig. 4 occur at low average readout photon number of $\bar{n}_r = 12, 19$, well within the power typically needed for high signal-to-noise dispersive readout of superconducting qubits [27].

We will now compute the transition probability of the p-MIST effect shown in Fig. 4(b). This choice was made based on a larger avoided crossing for (b) $\Delta_{ac} = 0.66$ as compared to (a) $\Delta_{ac} = 0.12$. For this
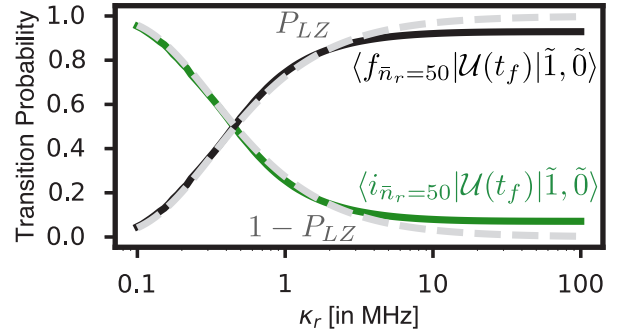

FIG. 5. Adiabatic (green) and diabatic (green) transition probability against the parameter κ_r which determines the change in drive strength $\xi_{\mu/\phi} = 2g_{\mu/\phi}\sqrt{\bar{n}_r(t)}$ where $\bar{n}_r(t)$ follows Eq. 8. Here, $|f_{\bar{n}_r=50}\rangle$ and $|i_{\bar{n}_r=50}\rangle$ are the final states in the end of branch analyses for $|\tilde{2}, \tilde{1}\rangle$ and $|\tilde{1}, \tilde{0}\rangle$, respectively, at $\omega_d = 9.05$ GHz. The Landau-Zener probability (P_{LZ}) for the avoided crossing in Fig. 4(b) is marked in gray.

analysis, instead of linearly increasing the drive power of a driven fluxonium circuit, we assume a time dependence of the average readout photon number of

$$\bar{n}_r(t) : \bar{n}_r(1 - e^{-\kappa_r t/2})^2, \qquad (8)$$

which includes a ring-up time of $1/\kappa$, according to the readout resonator bandwidth [19–21]. This equation computes the occupation of the readout resonator under a drive with a decay rate of κ_r.

We first use Hamiltonian dynamics to compute the transition probability as the overlap of the initial state $|\tilde{1}, \tilde{0}\rangle$ evolved under the unitary $U = e^{i\hat{H}_{s.c.}t}$ with the Floquet branch of the two states $|i\rangle = |\tilde{1}, \tilde{0}\rangle$ and $|f\rangle = |\tilde{2}, \tilde{1}\rangle$, involved in the transition. The system is evolved for a time $t_f = \frac{10}{\kappa_r}$ such that the readout mode reaches the steady state population. Varying κ changes the probability of transitions, plotted in Fig. 5. The overlap with 'i' represents the probability of an adiabatic transition while the probability of a

diabatic transition is given by the curve plotting the overlap against 'f'. We see that there is a significant probability of an adiabatic transition $\kappa_r \leq 1$ MHz, the target readout decay parameter (see Table II).

We also use the numerically-computed gaps in the quasi-energies to evaluate the Landau-Zener (LZ) probabilities P_{LZ}, using the method described in Ref. [29] (for details see App. C 4). Unlike the case of transmons Ref. [21] we do not find perfect agreement in these two cases. This indicates that the two-state physics captured by Landau-Zener transitions may not be correct for studying the strengths of fluxonium transitions. As $\kappa_r \to \infty$ the states seem to saturate to a superposition of $i - f$ since the green and black curves always sum up to 1. Note that, similar to the Hamiltonian dynamics the population exchange plots in Fig. 4(b) also show that the green and black curves do not

We have confirmed that an observed p-MIST can have significant probability during a fluxonium qubit readout. While this effect will directly affect the readout performance for our chosen set of readout parameters, we will now analyze its impact on the qubit coherence.

C. Qubit Dephasing post-Readout

Implications of p-MIST can be fatal even *after* the readout pulse is executed, in the context of a larger quantum circuit where the fluxonium mode is used as a qubit. In general, the parasitic modes are long-lived, with internal quality factors of $\sim 10^4$ [13, 33]. We have confirmed that dephasing due to the detuned drive and thermal effects is negligible (see App. C 5). However, spurious excited state population of the parasitic mode introduced by p-MIST during readout can induce correlated dephasing of the qubit, through the large dispersive interaction $\chi_{\mu\phi}/2\pi \sim 1$ MHz (see Table I). If the parasitic mode is excited, the qubit accumulates a phase at a constant rate $\chi_{\mu\phi}\bar{n}_\mu$, in the absence of any decay i.e. infinite internal quality factor Q_μ. This error can be measured and corrected for, given the knowledge of $\bar{n}_\mu$. For a finite Q_μ, the parasitic mode decays at a rate $\kappa_\mu = Q_\mu/\omega_\mu$ such that the qubit dephasing is no longer deterministic but a Poissonion process which relies on the random decay of the parasitic mode. Now, we will analyze this effect due to p-MIST induced excitation in the parasitic modes.

Post the readout pulse in transition 9 (see Fig. 4(b)) for $\kappa_r = 1$ MHz, we can reset the fluxonium subspace to, say, the qubit state $|+\rangle = \frac{|0\rangle_\phi + |1\rangle_\phi}{\sqrt{2}}$. The parasitic mode, however, remains in the excited state $|1\rangle_{\mu=2}$ with some probability. To emulate the effect of this transition, we perform a master equation simulation of a toy model where a disjoint qubit-cavity state $|+, \bar{n}_\mu\rangle$ is evolved under the Hamiltonian $H = \chi_{\phi\mu}\hat{a}_\mu^\dagger \hat{a}_\mu \sigma_z$. During this evolution, the cavity (here, the parasitic mode) suffers dissipation under the decay operator $\sqrt{\kappa_\mu}\hat{a}_\mu$. We plot in Fig. 6 the infidelity of the qubit state with the $|+\rangle$ state, after the parasitic mode reaches a steady state at $T_f = 10/\kappa_\mu$, for various Q_μ
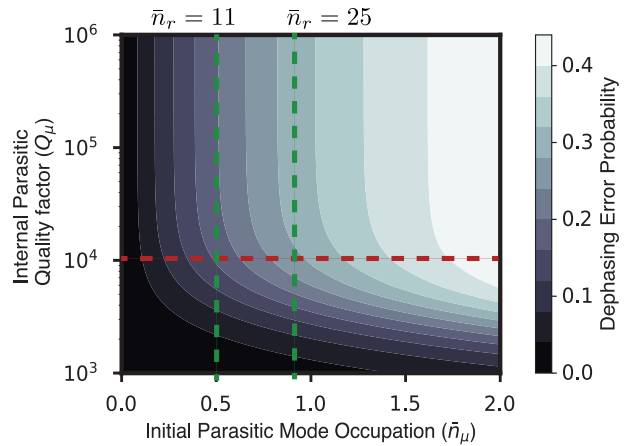

FIG. 6. Dephasing error probability due to random decay of an excited parasitic mode after p-MIST at finite Q_μ. The horizontal red line shows the quality factor quoted in [13]. The green lines show the dephasing error probability for transition 9 (see Figs. 4(b) and 5) at different average readout photons ($\bar{n}_r$).

and $\bar{n}_\mu$. Specifically, we find that for an internal quality factor Q_μ of 10^4 and population of $\langle n_\mu \rangle = 0.5$ in the parasitic mode $\mu = 2$ is needed to introduce a dephasing error probability, ~ 0.2, which is already past the threshold of surface code decoders [34]. Given that the population of the parasitic modes is about $\bar{n}_\mu \sim 0.5$ at a readout power of ~ 11 photons, well within the signal to noise ratio [27], we expect that qubit coherence can be limited by p-MIST in circuit designs which do not anticipate them.

Thus, we have provided quantitative evidence, with the help of various methods used in these analyses, that p-MIST processes can limit the performance of a fluxonium qubit architecture, without careful consideration of the parasitic modes during circuit design. In the next section, we will analyze the range of various mode frequencies and coupling strengths responsible for these effects.

IV. EFFECTS OF CIRCUIT MODIFICATIONS ON P-MIST

The p-MIST processes shown in the previous section can be mitigated in various ways, by adjusting the qubit frequency, readout resonator frequency, and parasitic mode frequencies, as well as reducing parasitic mode and qubit coupling strengths. In this section, we explore the impact of each of these components individually. All equations analyzed in this section were derived in Ref. [26] for the circuit in Fig. 2, and we have extended these results to circuits with different grounding configurations in App. A.

A. Coupling Strengths

The strong coupling between the qubit and the parasitic mode is primarily responsible for p-MIST processes. Here, we show evidence of this, via Flo-

quet simulations where various coupling constants are changed to zero to analyze their significance. Fig. 7 compares Floquet plots for the initial state $|\tilde{1}, \tilde{0}\rangle$ under different coupling conditions. Fig. 7(b) shows that $g_{\phi r}$ alone does not cause significant transitions or p-MIST processes without $g_{\phi\mu}$. This is evident from the absence of all parasitic transitions $(8, 9)$ and no streak or sharp change in color indicating parasitic mode excitations in the bottom panel. The parasitic mode population in the absence of this coupling is restricted to $\bar{n}_\mu = 10^{-4}$. Turning both parasitic couplings (not shown here) off completely removes any population from the parasitic mode. For full Floquet landscape with quasi-energy see App. B 2. Therefore, reducing the coupling strength $g_{\phi\mu}$ is a potential path to mitigating p-MIST processes.
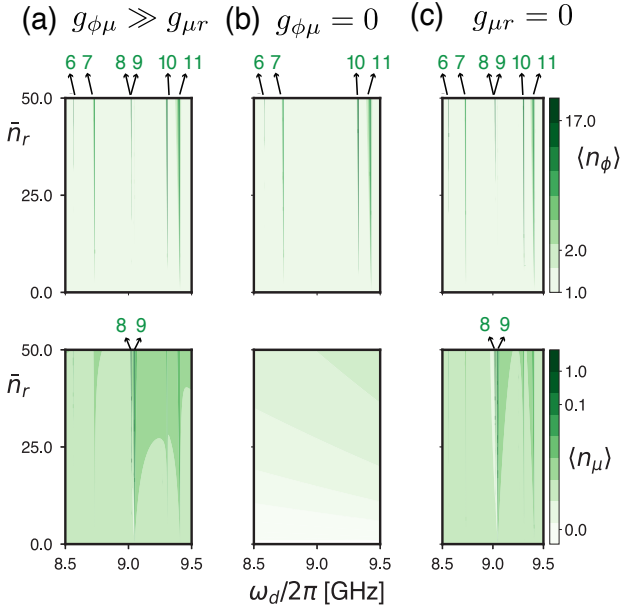
FIG. 7. Floquet Simulations for the circuit parameters in Table I due to the various coupling terms in Eq. 3. The marked transitions show the MIST processes observed in Fig. 3. **(a)** Same as Fig. 3(b). **(b)** Zero parasitic mode coupling to the qubit. **(c)** Zero parasitic mode coupling to the readout. Same as before the Floquet figures are plotted in log scale for visual aid to the marked transitions.

Here, we analyze the dependence of these coupling strengths on circuit and readout parameters. As derived in App. A and given in [26], the coupling strength $g_{\phi\mu}$ is

$$g_{\phi\mu} = \sqrt{\frac{2}{N}} \frac{\tilde{E}_c^\phi \tilde{E}_{c,\mu}^e c_\mu}{E_{g_j} s_\mu^2} \cdot N_{\phi ZPF} \cdot N_{\mu ZPF} \quad (9)$$

where $c_\mu = \cos\frac{\pi\mu}{2(N-1)}$, $\tilde{E}_c^\phi, \tilde{E}_{c,\mu}^e$ are the qubit and parasitic mode charging energies, respectively, and $N_{\phi/\mu, ZPF}$ are the zero-point fluctuation values for the qubit and parasitic modes. Expressions for $\tilde{E}_{c,\mu}^e$ can be found in Eq. 13, $\tilde{E}_c^\phi, N_{\phi/\mu, ZPF}$ can be found in App. B while all the other parameters are given in Table I.

By observation, suppressing the parasitic capacitance to ground near the junction array suppresses the qubit-parasitic coupling $g_{\phi\mu}$. However, this is constrained by practical limits of around 0.1 fF per junction due to the gap to the ground plane. For the parasitic modes with strongest coupling to the qubit $\mu \ll N$, the large N limit with $c_\mu \approx 1$ yields

$$\tilde{E}_{c,\mu}^e \approx E_{g_j} s_\mu^2, \quad \tilde{E}_c^\phi \propto \frac{1}{N^2} \implies g_{\phi\mu} \propto \frac{1}{N^{5/2}}. \quad (10)$$

These dependencies are plotted in Fig. 14 of App. B. The trend with respect to N is not so straight forward. Note that changing N changes the target inductance of the qubit. Keeping the same inductance as N changes requires one to increase E_{J_j} by the same factor as N. To keep the E_{J_j}/E_{C_j} ratio the same this leads to an increase in E_{C_j}, thus extending our argument for large N even further. Thus, both these tasks (increasing N, decreasing $C_{g,j}$) are hard at hand.

B. Mode Frequencies

We can estimate the resonance conditions for a p-MIST effect by identifying energy-conserving processes, where x photons are converted into a transition $\tilde{\Delta}_{if,y}$ in the hybridized eigenspace of the fluxonium and parasitic mode $\mu = 2$. Here, $\tilde{\Delta}_{if,p}$ is the transition energy between levels $|\tilde{i}, \tilde{m}\rangle$ and $|\tilde{f}, \tilde{n}\rangle$ such that $|m - n| = y$. In the disjoint Hilbert space, this equation can also be interpreted as a process where x readout photons convert into y parasitic mode photons and a fluxonium excitation $|i\rangle_\phi \leftrightarrow |f\rangle_\phi$ ($\Delta_{if} = |E_f - E_i|$). To guide intuition for understanding the spectrum of resonance conditions, we plot such energy-conserving processes in Fig. 8, for the lowest-order case of $\mu = 2$, that satisfy

$$|x\omega_r - \tilde{\Delta}_{if,y}| \approx |x\omega_r - (y\omega_\mu + \Delta_{if})| \leq 25 \text{ MHz}, \quad (11)$$

where a buffer of 25 MHz is allowed to accommodate for Stark shift (see App. C 2).

The energy profile profile in Fig. 8 shows us the regions where up to four-photon processes will be prominent when starting in one of the four lowest fluxonium levels involved in the readout. Note that there are downward transitions from $|2\rangle_\phi$ to $|1\rangle_\phi, |0\rangle_\phi$ in the fluxonium subspace, in the presence of parasitic modes, one of which was captured in transition 15 of Table I. To emphasize the correctness of these predictions we mark all the transitions captured in the Floquet simulations (see Sec. III) in Fig. 8. The labels denote the number of readout photons (xr) and parasitic mode photons (yp) required for the transition in the fluxonium subspace, where a positive index denotes absorption while a negative index denotes emission. These labels correspond to the disjoint subspaces for simplified representation but the energy conservation uses the eigen-energies of the hybridized eigenstates of H_0 (see Eq. 5). For example, transition 2 emits 4 readout photons which are converted into 2 parasitic mode photons, absorbed by the mode $\mu = 2$, and the transition $|0\rangle_\phi \leftrightarrow |4\rangle_\phi$ in the fluxonium subspace. The equation indicates that a large gap between ω_d and ω_μ would require a large m to trigger
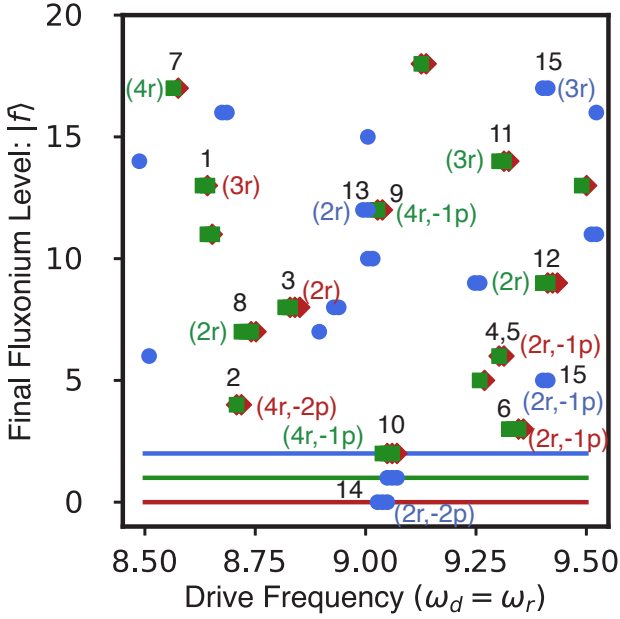
FIG. 8. Energy conserving processes $|\tilde{i}, \tilde{0}\rangle \leftrightarrow |\tilde{f}, \tilde{y}\rangle$ for Eq. 11 for $x \leq 4, y \leq 2, j \leq 20$ and $i = 0$ (red), $i = 1$ (green), $i = 2$ (blue). The horizontal lines indicate the initial state for each color for visual aid. Labels in black correspond to transition # listed in Table III. Colored labels $(x\mathrm{r}, -y\mathrm{p})$ show the number of readout photons absorbed (x) and the number of parasitic mode $(\mu = 2)$ photons emitted (y) in the transition.

FIG. 9. Floquet simulations at lower readout frequencies using circuit parameters quoted in Tables I and II for branch analysis starting in the dressed hybridized eigenstate $i = |\check{k}, \tilde{0}\rangle$, with maximum overlap to the unhybridized states $|k\rangle_\phi \otimes |0\rangle_{\mu=2}$. The figures are plotted in linear scale, unlike Fig. 3, making any streak due to significantly weaker transitions ($\Delta_{ac} < 1\ \mathrm{KHz}$) unnoticeable.

a p-MIST effect. We verify this intuition for different ranges of the various mode frequencies.

    a. Drive Frequency (ω_d): If $\omega_d \gg \omega_{\mu=N-1}$, the most fatal case would be excitation of a strongly coupled low-frequency parasitic mode to large n leaving just enough energy to produce excitation f in the Fluxonium subspace of significant charge matrix elements (see Fig. 12). However such large excitations in the parasitic modes would be less probabilistic. A proper investigation of this case requires a large Hilbert space and is beyond the scope of this work. A low frequency readout, on the other hand, would incur a large m and can have similar impact. We give the Floquet figure corresponding to a low frequency readout in Fig. 9 which looks severely more populated compared to Fig. 3. It is important to compare the rates of such transitions, however, the increase can be explained around 6 GHz. The rear end of this frequency range is the same as the plasmon energy and half the parasitic mode $\mu = 2$ frequency. This logic already indicates that $5.5 - 6$ GHz would be a bad range of frequencies for the current choice of parameters. However, for the purpose of readout, a lower ω_d is not favorable due to thermal effects, and hence not analyzed further in this work.

    b. Parasitic Mode Frequency: Another approach towards mitigating p-MIST processes is to adjust ω_μ so that $\omega_\mu \gg \omega_r$ for $\mu = 2$, potentially improving the circuit. This is feasible with granular-aluminum (GrAl) inductive shunts, though they are lossy [27]. Recent efforts are being applied towards improving GrAl shunts.

    For the JJA parameters, to provide some quantita-

tive arguments in this direction we discuss the dependency of ω_μ for even parasitic modes (e) on various circuit variables.

$$\frac{\omega_\mu^e}{2\pi} = \sqrt{8 E_{c,\mu}^e E_{J_j}}, \quad \text{where} \tag{12}$$

$$E_{c,\mu}^e = \left[\frac{1}{E_{C_j}} + \frac{1}{4 E_{g_j} s_\mu^2}\right]^{-1}. \tag{13}$$

Here, $s_\mu = \sin(\frac{\pi\mu}{2(N-1)})$. Here, $E_{c,\mu}^e$ is the charging energy of an even parasitic mode. All other variables used are defined in Table I. For parasitic modes with strong coupling, $\mu \ll N$, for large N, the charging energy is $\tilde{E}_{c,\mu}^e \approx 4 E_{g,j} s_\mu^2$, which is inversely proportional to N^2 and directly proportional to E_{g_j}. Again, a smaller parasitic ground capacitance C_{g_j} increases the parasitic mode charging energy, and thus desirably increasing its frequency. However, in contrast with the case of coupling strength $g_{\phi\mu}$, a larger N leads to lower frequencies for these modes, which is unfavorable. Fig. 14 in App. B shows the dependence of charging energy of parasitic modes as well as qubit modes with respect to parasitic ground capacitance. As stated before in Sec. IV A, the ground capacitance $C_{g,j}$ is fixed while the impact of decreasing N would require consideration of nonlinear corrections as well as fixed inductance, thus, again making these changes difficult.

    In the previous sections we focused on ~ 30 MHz fluxonium frequency. To extend our results to other experiments, we consider another circuit inspired by parameters in [6] and show p-MIST processes in a 236 MHz fluxonium. The parasitic mode frequency of the $\mu = 2$ mode is $\omega_{\mu=2} = 15.51$ GHz. The coupling strengths are as follows, $g_{\phi r} = 37$ MHz, $g_{\phi\mu} = 216$ MHz, $g_{\mu r} = 6$ MHz. The plasmon fre-

quency is $\omega_{12} = 5.40$ GHz. Importantly, here we only plot results for $|\tilde{0}, \tilde{0}\rangle$ and $|\tilde{1}, \tilde{0}\rangle$ because given Ref. [6] uses only the first two levels for readout as well as computation. The detailed circuit parameters are given in App. D. The truncation for the simulation of this alternate circuit is discussed is shown in App. D. Even though the coupling strengths for these circuit parameters are on par with Table I, since the parasitic mode frequency of the even mode $\mu = 2$ is larger by ~ 4 GHz, we expect fewer p-MIST processes in the drive frequency range analyzed in Fig. 3.
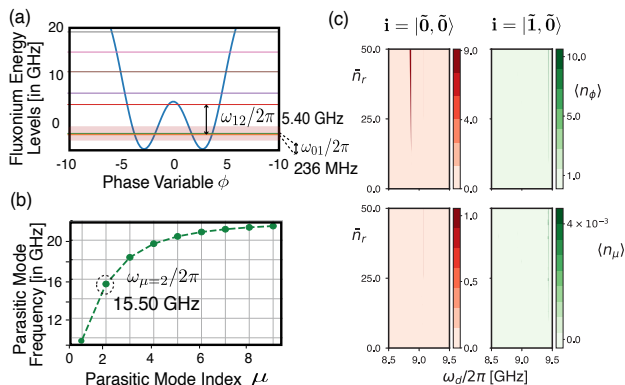
FIG. 10. Floquet analysis with alternate JJA fluxonium parameters. **(a)** Fluxonium energy spectrum. **(b)** Parasitic mode frequencies. **(c)** Floquet simulations for the branch analysis of the computational states [35]. Circuit parameters for this circuit are discussed in Sec. IV B and App. D. The Floquet figures are plotted in linear scale unlike Fig. 3, making any streak due to significantly weaker transitions ($\Delta_{ac} < 1$ KHz) unnoticeable.

Fig. 10 shows that the ratio of observed MIST (3) and p-MIST (1) effects is indeed lower for this alternate circuit. In fact, the one p-MIST observed in the Floquet profile $|\tilde{0}, \tilde{0}\rangle \leftrightarrow |\tilde{4}, \tilde{1}\rangle$ occurs at $\bar{n}_r = 25$ and has the quasi-energy gap of $\Delta_{ac} = 0.13$ MHz at the avoided crossing. This transition, thus, seems comparable rate to transition 8 (see Fig. 4(a)) which is much weaker compared to transition 9 (see Fig. 4(a)), as observed in Sec. III B. The corresponding Landau-Zener probabilities and explicit transitions with quasienergies for the Floquet profile in Fig. 10 can be found in App. D. However, a detailed understanding of this Floquet profile, including rate calculations, is necessary to make proper claims in relation to severely reduced MIST processes, and is left as future direction.

V. CONCLUSION AND FURTHER WORK

In this work, we have analyzed the impact of parasitic modes on driven JJA fluxonium qubit. This work shows that transitions in a fluxonium circuit triggered by a parasitic mode of the JJA can occur with considerable rates from coupling of the parasitic modes with the qubit mode. Our results, while simulated for a driven fluxonium circuit can give intuition related to MIST processes during a readout pulse. We show this simplification from the readout circuit Hamiltonian and justify that our claims hold for readout induced

state transitions. The parallel circuit considered in this work utilizes a specific symmetry which removes the coupling between the lowest frequency mode and the qubit. We show that this symmetry is preserved even if the readout resonator is coupled to a floating or grounded fluxonium at a single point. Our analysis considers fluxonium at the sweet spot which introduces additional symmetries forbidding transitions between parity-conserving states via first-order transitions. Despite these various symmetries and our modest assumption of no self-nonlinearity in the JJA or the readout, our results show that a strong coupling of parasitic modes to the qubit mode still triggers parasitic transitions at low average readout photons. We call these transitions parasitic-MIST or p-MIST, inspired by the term MIST for measurement-induced-state-transitions. Not only does p-MIST lower the onset of MIST processes to ~ 10 readout photons but it also significantly dephases the qubit, both of which directly limit the readout fidelity [36].

We analyze the trend in p-MIST for various drive frequencies, parasitic mode frequencies, coupling constants, and circuits with two different qubit frequencies equal to ~ 30 and ~ 300 MHz. The assumptions we make are crucial to our MIST analysis. Increasing N can reduce the nonlinearity of the parasitic modes, with insights provided in Sec. IV. We also neglect the self-nonlinearity of the readout mode which has been a common practice in recent MIST-related analysis [17, 20, 21]. While the effects of nonlinearity in parasitic and readout modes can have significant impact on the readout fidelity, Floquet simulations including self-nonlinearity of these modes is beyond the scope of our work. Analysis of a disordered array could also be an interesting extension of our work as it may lead to lower coupling between the qubit and the parasitic modes.

To advance practical implementation and reduce fluxonium MIST in the dispersive readout, we suggest adding noise to the Floquet framework [37] and linking our results to readout fidelity values using input-output theory. Future work should also incorporate the intrinsic nonlinearity of both the junction array modes and the readout mode. Mitigating parasitic mode excitations could involve varying junction energies along the array to localize collective modes, thereby altering the parasitic mode spectrum and reducing excitation probability. Alternative readout schemes like longitudinal readout or cloaking could also be explored [38–40]. Given the strong coupling between parasitic modes and fluxonium, these modes could potentially enhance fluxonium qubit readout. We propose using a feedline with a Purcell filter to tailor the spectrum and protect the qubit, reducing capacitive loading constraints.

Our results present a first analysis toward understanding the role of parasitic modes in the readout dynamics of a fluxonium circuit. Although the circuit parameters used in this work are closest to a fluxonium circuit, these results can be generalized to other high-anharmonic superconducting circuits with similar mode frequencies.

VI. ACKNOWLEDGMENTS

Appendix A: Single-Point Connections

Fluxonium Parameters ($\mu = 2$)	H_1 Parallel Circuit	H_2 Floating Fluxonium	H_3 Grounded Fluxonium
$g_{\phi\mu}$	157 GHz	161 GHz	158 GHz
$g_{\mu r}$	4.223 MHz	3.971 MHz	3.128 MHz
$\chi_{\phi,\mu}$	-1.1 MHz	-1.3 MHz	-1.1 MHz
$\delta\omega_{01,\mu}$	0.4 MHz	0.45 MHz	0.41 MHz

TABLE IV. Fluxonium parameters with the lowest frequency parasitic mode with non-zero coupling to the qubit and readout $\mu = 2$. Here we quote the frequency of the fluxon transition between the lowest two levels (ω_{01}) and the plasmon transition between the first and second levels (ω_{12}). For the dispersive Hamiltonian obtained for each circuit in Fig. 11(a-c), we quote the dispersive shift due to readout as χ_r. The values in this table have been experimentally verified for H_1. The frequency of this mode is $f_\mu = 12.063$ GHz. We give the coupling strengths between the qubit-readout $g_{\phi\mu}$, readout-parasitic $g_{\phi r}$, parasitic-qubit $g_{\mu r}$ modes. We also give the stark shift $\chi_{\phi\mu}$ and frequency correction $\delta\omega_{01,\mu}$ on the two-level system realized by this fluxonium circuit in the dispersive regime. Here the values of $g_{\phi r}, \chi_{\phi r}, \omega_{\mu=2}$ have been verified experimentally for H_1.

The fluxonium readout circuit shown can have several modifications and each can affect various parameters associated with the efficiency of a fluxonium readout circuit as we proceed to show in this work. Here, in Fig. 14 we present two modifications to the parallel circuit shown in Fig. 2 with different grounding options for the fluxonium circuit. We will refer to these three circuit choices as H_1 : (Parallel circuit, see circuit in Fig. 2), H_2 : (Floating fluxonium, see left circuit in Fig. 14), H_3 : (Grounded fluxonium, see right circuit in Fig. 14). Note that each parameter in Table. IV is significantly different for the three circuits. We adjust the coupling capacitance C_c and the total capacitance of the phase slip junction E_{C_p} (by modifying C') to achieve the same qubit frequency ω_{01}, plasmon frequency ω_{23}, qubit-readout coupling constant $g_{\phi\mu}$ and qubit-readout dispersive shift $\chi_{\phi r}$ for the three circuits as given in Table. I. These modifications yield for circuit (b)$E_{C_p} = 0.83$ GHz, $E_{C_c} = 3.82$ GHz (c) $E_{C_p} = 0.80$ GHz,$E_{C_c} = 4.70$ GHz. Table. IV gives values of the various circuit parameters across the three circuits computed analytically using the expressions given in App. B. We note that upon adjusting the qubit parameters, all circuit parameters are similar in the three circuits. We find that, if the differential capacitance C and coupling capacitance C_c are altered such that qubit frequency and qubit-readout coupling are same across all three circuits, the parasitic mode effects are bound to have the same effect given our assumptions of ordered array and no self-nonlinearity in parasitic modes. Hence, we do not expect any change in the MIST/p-MIST processes for single-point connected circuits in the hangar geometry in comparison to what has already been shown in this work. To emphasize this, we plot the three types of coupling strengths across all circuits in Fig. 11(d) while other parasitic parameters are given in Table. IV. Note that, this symmetry prevents any coupling with the lowest-frequency parasitic mode ($\mu = 1$) in all three circuits, presence of which would have been potentially detrimental.

Here we will follow the recipe of Ref. [26] to derive Hamiltonians for circuits shown in Figs. 14(b,c). We will use the following notations defined in Table V. The Lagrangian corresponding to these circuits is a combination of the Lagrangians, $\mathcal{L}_g$ from the phase-slip junction (comprising of the junction with $E_J/E_C \sim 5 - 8$ and the capacitor C), $\mathcal{L}_g$ from the ground capacitances, $\mathcal{L}_R$ from the readout resonator and $\mathcal{L}_c$ due to the coupling capacitances C_c and the external voltage V. We mark the flux points across JJA using φ_0 and φ_N. We write the capacitive energy terms using $E_x = \frac{e^2}{2C_x}$ and the voltages of each island $\dot\varphi/2e$, such that, $\frac{1}{2}C\frac{\dot\varphi^2}{4e^2} = \frac{\dot\varphi^2}{16E_C}$. For simplicity, we have $C_{g,i} = C_g \quad \forall i$. The flux variables and voltage variables in the circuit are denoted by $\varphi_n = 2\pi\Phi_n/\Phi_0$ and $\dot\varphi_n = 2\pi V_n/\Phi_0$, respectively, where $\Phi_0 = h/2e$ is the superconducting flux quantum. We will use subscripts j, p for JJA and the phase-slip junction coordinates, respectively. The capacitance associated with the phase-slip junction is given by $\frac{1}{E_{C'}} = \frac{1}{E_C} + \frac{1}{E_C^j}$.

1. Floating Fluxonium Circuit

For H_2, Transforming the Lagrangian in Ref. [26], the following terms will remain the same in the case of floating fluxonium circuit, given the diagrams in the following sections.

$$\mathcal{L} = \mathcal{L}_{phase-slip} + \mathcal{L}_{JJA} + \mathcal{L}_g + \mathcal{L}_R + \mathcal{L}_C \tag{A1}$$

$$\mathcal{L}_{phase-slip} = \frac{(\dot\varphi_N - \dot\varphi_0)^2}{16E_{C'}} - E_{J_p}\cos(\varphi_0 - \varphi_N + \varphi_{ext}) \tag{A2}$$

$$\mathcal{L}_{JJA} = \sum_{n=1}^N \frac{(\dot\varphi_n - \dot\varphi_{n-1})^2}{16E_{C_j}^n} - E_{J_j}^n\cos(\varphi_n - \varphi_{n-1}) \tag{A3}$$

$$\mathcal{L}_R = \frac{\dot\varphi_-^2}{16E_R} - \frac{\varphi_-^2}{16E_R} \tag{A4}$$

$$\mathcal{L}_g = \sum_{n=0}^N \frac{\dot{\varphi_n}^2}{16E_g^n} \tag{A5}$$

Here, we will not assume that the capacitances to transmission line are infinite or that ground capacitance for the phase-slip junction and JJA. We will

FIG. 11. (a-c) Alternative readout circuits. (a) Parallel circuit, (b) Floating fluxonium, (c) Grounded fluxonium. Alternatives (b) and (c) require a single-point connection to the readout line V, unlike the parallel circuit in (a). We maintain the values for all circuit variables the same as used for the case of the parallel circuit in Fig. 2. (d) Absolute values of the coefficients of coupling terms in the Hamiltonian (in GHz). We can see that the parasitic modes couple to the qubit stronger than the qubit couples to the readout. The parasitic mode coupling to the readout is very slightly weaker in H_3 compared to H_1, H_2.

leave the value of $\varphi_\pm$ a variable in this case unlike the parallel circuit study we performed above.

$$\mathcal{L}_c = \frac{(\dot{\varphi}_{-1} - \dot{\varphi}_0)^2}{16E_c^1} + \frac{(\dot{\varphi}_{-1} - eV)^2}{16E_c^3} + \frac{(\dot{\varphi}_{-2})^2}{16E_c^4}, \quad (A6)$$

$$= \frac{\dot{\varphi}_0^2}{16E_c^1} + \frac{\dot{\varphi}_{-1}^2}{16}\left(\frac{1}{E_c^1} + \frac{1}{E_c^3}\right) + \frac{\dot{\varphi}_{-2}^2}{16E_c^4}$$

$$- \frac{\dot{\varphi}_0\dot{\varphi}_{-1}}{8E_c^1} - \frac{\dot{\varphi}_{-1}eV}{8E_c^3} + \mathcal{O}(V^2) \quad (A7)$$

Here, E_c^4 is the capacitance via which the readout resonator is grounded. Using the basis of (guage-invariant) phase difference,

$$\varphi_m - \varphi_0 = \sum_{l=1}^{m}\theta_l \quad (A8)$$

$$\sum_{m=0}^{N}\theta_m + \varphi_{ext} = 2\pi z, \quad z \in \mathbb{Z} \quad \text{"fluxoid quantization"} \quad (A9)$$

$$\varphi_{ext} = \pi, \quad (A10)$$

a. *Lagrangian* From using Eq. A5, we find that,

$$\dot{\varphi}_0 = E_t\left(\frac{\dot{\varphi}_{-1}}{E_c^1} - \sum_{n=1}^{N}\sum_{m=n}^{N}\frac{\dot{\theta}_n}{E_g^m}\right) \quad (A11)$$

$$\text{where} \quad E_t = \left(\frac{1}{E_c^1} + \sum_{n=0}^{N}\frac{1}{E_g^n}\right)^{-1}$$

$$\therefore \mathcal{L}_g + \mathcal{L}_c = \frac{\dot{\varphi}_{-1}eV}{8E_c^3} + \frac{\dot{\varphi}_{-1}^2}{16}\left(\frac{1}{E_c^1}\left(1 - \frac{E_t}{E_c^1}\right) + \frac{1}{E_c^3}\right)$$

$$+ \sum_{n=1}^{N}\frac{\dot{\varphi}_{-1}\dot{\theta}_n}{E_c^1}\left(\sum_{i=n}^{N}\frac{E_t}{8E_g^i}\right)$$

$$+ \sum_{m=1}^{N}\sum_{n=1}^{N}\dot{\theta}_m\dot{\theta}_n\left(\sum_{j=\max\{m,n\}}^{N}\frac{1}{16E_g^j}\right)$$

$$\left(1 - \sum_{i=\min\{m,n\}}^{N}\frac{E_t}{E_g^i}\right) \quad (A12)$$

We simplify the Lagrangian $\mathcal{L}_g + \mathcal{L}_c$ as

$$= \frac{\dot{\varphi}_{-1}eV}{8E_c} + \frac{\dot{\varphi}_{-1}^2}{16}\left(\frac{1}{E_c}\left(1 - \frac{E_t}{E_c}\right) + \frac{1}{E_c}\right)$$

$$+ \sum_{n=1}^{N}\left(\frac{\dot{\varphi}_{-1}\dot{\theta}_n}{E_c}\right)(N - n + 1)\frac{E_t}{8E_g} + \frac{(\dot{\varphi}_{-2})^2}{16E_c^4}$$

$$+ \sum_{m=1}^{N}\sum_{n=1}^{N}\dot{\theta}_m\dot{\theta}_n\frac{(N - \max\{m,n\} + 1)\min\{m,n\}E_t}{16E_g^2} \quad (A13)$$

This expansion shows that the parasitic couplings depend on the ground capacitance due to terms like $\dot{\theta}_m\dot{\theta}_n$ while the coupling capacitance comes into picture only via couplings with the readout resonator mode.

b. *Collective Modes* We now transform to a new set of variables $\{\phi, \zeta_1, ..., \zeta_{N-1}\}$, also known as the difference modes μ and their amplitudes ξ_μ,

$$\theta_m = \phi/N + \sum_\mu W_{\mu m}\xi_\mu, \quad (A14)$$

001

e. Hamiltonian: We can see that there is no choice of $\dot{\varphi}_\pm$ such that the parasitic coupling between the readout resonator and fluxonium can be cancelled without eliminating the coupling between the qubit and readout resonator. Note that, this expression assumed $C_g^0 = C_g^N = C_g^1.. = C_g^{N-1}$, such that $\frac{N+1}{E_g} = \frac{1}{E_g} - \frac{1}{E_c}$. The coupling between the qubit and the readout is same as the parallel circuit if $E_g << E_c$ with a lower N. We drive the readout resonator, such that, $\dot{\varphi}_- = 2eV$ (the sign of the voltage value has been changed because in this circuit φ_{-1} will be connected to V and not $-V$, just for simplicity).[SS: Check the sign of the eV terms]

$$
\begin{aligned}
\mathcal{L} = &\frac{\dot{\varphi}_+^2}{64E_c}\left(2 + \frac{(N+1)E_t}{E_g}\right) + \frac{\dot{\varphi}_+ eV}{16E_c}\left(\frac{3}{2} + \frac{E_t}{E_c}\right) \\
&- \frac{(N+1)E_t}{32E_gE_c}\dot{\phi}eV + \frac{(N+1)E_t}{64E_gE_c}\dot{\phi}\dot{\varphi}_+ \\
&- \frac{E_t}{16E_gE_c}\sum_\mu \frac{c_\mu o_\mu}{\sqrt{2N}s_\mu^2}\dot{\xi}_\mu eV \\
&+ \frac{E_t}{32E_gE_c}\sum_\mu \frac{c_\mu o_\mu}{\sqrt{2N}s_\mu^2}\dot{\xi}_\mu\dot{\varphi}_+ + \mathcal{O}(e^2V^2) \\
&+ \Big[(M_{00} + G_{00})\dot{\phi}^2 + 2\sum_\mu (M_{0\mu} + G_{0\mu})\dot{\phi}\dot{\xi}_\mu \\
&+ \sum_{\mu,\nu}(M_{\mu\nu} + G_{\mu\nu})\dot{\xi}_\mu\dot{\xi}_\nu\Big] - \mathcal{U}
\end{aligned}
\tag{A27}
$$

This Lagrangian can be used to analyze effects in floating readout case. However, for simplicity, we can again just like the previous case, assume $C^3 = C^4 = 0$ which makes the floating resonator grounded. Ideally this choice should not affect the analysis until we study the effects of a driven readout resonator (even then the intuition is that the ground capacitance should not make things worse [SS: Check this intuition when analyzing a driven resonator. Also, we can check if changing $C_g^N = E_C^2 = E + C^1$ brings the effect of Floating resonator closer to a parallel circuit. It will never be similar because we have one less ground capacitance term here.]). Currently this is equivalent to eliminating all terms with E_c^3, E_c^4 and using $\dot{\varphi}_{-2} = 0, \dot{\varphi}_{-1} = -2eV$. Thus, $\varphi_+ = \varphi_- = -2eV$.

$$
\begin{aligned}
= &- \frac{(N+1)E_t}{16E_gE_c}\dot{\phi}eV - \frac{E_t}{8E_gE_c}\sum_\mu \frac{c_\mu o_\mu}{\sqrt{2N}s_\mu^2}\dot{\xi}_\mu eV \\
&+ \Big[(M_{00} + G_{00})\dot{\phi}^2 + 2\sum_\mu (M_{0\mu} + G_{0\mu})\dot{\phi}\dot{\xi}_\mu \\
&+ \sum_{\mu,\nu}(M_{\mu\nu} + G_{\mu\nu})\dot{\xi}_\mu\dot{\xi}_\nu\Big] - \mathcal{U}
\end{aligned}
\tag{A28}
$$

Next, we write the Legendre transformation using the velocity vectors and matrices,

$$
\begin{aligned}
p_\phi = \frac{\partial \mathcal{L}_{\kappa o}}{\partial \dot{\phi}} = &2(M_{00} + G_{00})\dot{\phi} + \sum_\mu (M_{\mu 0} + G_{\mu 0})\dot{\xi}_\mu \\
&- \frac{(N+1)E_t}{16E_gE_c}eV
\end{aligned}
\tag{A29}
$$

$$
p_{\xi_\mu} = \frac{\partial \mathcal{L}_{\kappa o}}{\partial \dot{\xi}_\mu} = (M_{0\mu} + G_{0\mu})\dot{\phi} + 2\sum_\nu (M_{\mu\nu} + G_{\mu\nu})\dot{\xi}_\nu
$$

$$
- \frac{E_t}{8E_gE_c}\sum_\mu \frac{c_\mu o_\mu}{\sqrt{2N}s_\mu^2}eV
\tag{A30}
$$

Here, the even and odd sectors are not decoupled due to the eV term which will eventually act as the readout resonator mode. The even and odd sectors can be diagonalized independently, such that a rotation on the odd sectors does not affect the even sectors. This is contrary to the case of Eq. 77 in [26] where the rotation of odd sectors affects the even sectors. This is because in that case $G_{0\mu}$ was changed to being dependent on odd as well as even sectors. However, here, only the $\mathcal{L}_V$ term has changed. Thus, if the following condition is satisfied,

$$
\frac{\tilde{E}_c^\phi \tilde{E}_{c,j}^e c_i c_j}{32N E_g^2 s_i^2 s_j^2} << 1 \implies \frac{4E_g \tilde{E}_c^\phi c_i c_j}{32N E_g^2 s_i^2} << 1
\tag{A31}
$$

$$
\implies \frac{4\tilde{E}_c^\phi N}{8E_g \pi^2 \mu\nu} << 1 \implies N << 8\pi^2 \frac{E_g}{\tilde{E}_c^\phi}
\tag{A32}
$$

we can carry out the exact same procedure as Ref. [26] to simplify the inversion of matrix for the Legenrdre transformation and obtain the Hamiltonian as follows. [SS: Check both the matrix inverse requirement and condition in this case again]. Thus, we get the Hamiltonian as,

$$
\begin{aligned}
H_2 = &4\bar{E}_c^\phi p_\phi^2 + \sum_{\mu=1}^{N-1} 4\tilde{E}_{c,\mu}^{e/o}p_\mu^2 \\
&+ 2\sum_{\mu=1}^{N-1} \frac{\bar{E}_c^\phi \tilde{E}_{c,\mu}^{e/o} c_\mu o_{\mu+1}}{\sqrt{2N}E_g s_\mu^2}p_\phi p_\mu \\
&- \bar{E}_c^\phi p_\phi eV\Big[\frac{(N+1)E_t}{2E_gE_c} + \frac{E_t^2 \tilde{E}_{c,\mu}^{e/o}}{8E_g^2 E_c^2}\Big(\frac{c_\mu^2 o_\mu}{2Ns_\mu^4}\Big)\Big] \\
&- \sum_{\mu=1}^{N-1} \frac{\bar{E}_c^\phi \tilde{E}_{c,\mu}^{e/o} c_\mu o_{\mu+1}}{\sqrt{2N}E_g s_\mu^2}\Big[\frac{(N+1)E_t}{8E_gE_c}\Big]p_\mu eV \\
&+ E_{J_p}\cos\phi + \frac{E_L}{2}\phi^2 + \frac{E_{J_j}}{2}\sum_{\mu=1}^{N-1}\xi_\mu^2 - \frac{\varphi_-^2}{16E_R}
\end{aligned}
\tag{A33}
$$

where the variables $\tilde{E}_{c,\mu}^e$ are same as before and $\tilde{E}_{c,\mu}^o$ is the diagonalized charging energy of odd sectors. $\tilde{E}_{c,\mu}^{e/o}$ denotes that the term will be $\tilde{E}_{c,\mu}^o$ for odd μ and $\tilde{E}_{c,\mu}^e$ for even μ. Thus, we can see that by not preserving the symmtery we only have the extra odd sector term interacting with the readout resonator. However, we can see that this term is extremely small. $\mathcal{U}$ remains the same as the parallel case. Thus, in terms of types of couplings there might not be major differences, however, value of $\bar{E}_c^\phi = (G_{00} + M_{00})^{-1}$ changes since G_{00} has changed. This change can also be diminished with increasing N. Thus, for large enough N, this circuit is the same as the parallel circuit. [SS: Write this in terms of previous format of H_ϕ]

2. Grounded Fluxonium Circuit

For H_3, the constraint $\dot{\varphi}_N = 0$ yields

$$\mathcal{L} = \mathcal{L}_{phase-slip} + \mathcal{L}_{JJA} + \mathcal{L}_g + \mathcal{L}_R + \mathcal{L}_C \tag{A34}$$

$$\mathcal{L}_{phase-slip} = \frac{\dot{\varphi}_0^2}{16E_{C'}} - E_{J_p}\cos(\varphi_0 + \varphi_{ext}) \tag{A35}$$

$$\mathcal{L}_{JJA} = \sum_{n=1}^{N} \frac{(\dot{\varphi}_n - \dot{\varphi}_{n-1})^2}{16E_{C_j}^n} - E_{J_j}^n \cos(\varphi_n - \varphi_{n-1}) \tag{A36}$$

$$\mathcal{L}_R = \frac{\dot{\varphi}_-^2}{16E_R} - \frac{\varphi_-^2}{16E_R} \tag{A37}$$

$$\mathcal{L}_g = \sum_{n=0}^{N-1} \frac{\dot{\varphi}_n^2}{16E_g^n} \tag{A38}$$

Here, we will not assume that the capacitances to transmission line are infinite or that ground capacitance for the phase-slip junction and JJA. We will leave the value of $\varphi_\pm$ a variable in this case unlike the parallel circuit study we performed above. The grounding of fluxonium yields an additional condition to the fluxoid condition $\varphi_N = c$, a constant which implies,

$$\varphi_0 = c - \sum_{l=1}^{N} \theta_l \implies \dot{\varphi}_0 = -\sum_{l=1}^{N} \dot{\theta}_l \tag{A39}$$

This used to be our qubit in the definition of collective modes in this article. However, in this case there are only $N-1$ modes, such that the collective modes are defined as,

$$\phi = c + \sum_{l=1}^{N-1} \theta_l \implies \dot{\phi} = -\dot{\varphi}_0 \tag{A40}$$

[SS: Is there a different mechanism we need to use here? (1) We should only have N-1 modes] Since one of the dynamic variables are fixed we only have $N-1$ modes, thus,

$$\mathcal{L}_{phase-slip} = \frac{(\sum_{m=1}^{N-1} \dot{\theta}_m)^2}{16E_{C'}} + E_{J_p}\cos\left(\sum_{m=1}^{N}\theta_m + \varphi_{ext}\right) \tag{A41}$$

$$\mathcal{L}_{JJA} = \sum_{n=1}^{N-1} \frac{\dot{\theta}_n^2}{16E_{C_j}^n} - E_{J_j}^n \cos\theta_n \tag{A42}$$

$$\mathcal{L}_R = \frac{(\dot{\varphi}_{-1} - \dot{\varphi}_{-2})^2}{16E_R} - \frac{(\varphi_{-1} - \varphi_{-2})^2}{2L_R} \tag{A43}$$

$$\mathcal{L}_g = \frac{\dot{\varphi}_0^2}{16E_g^0} + \sum_{n=1}^{N} \frac{(\dot{\varphi}_0 + \sum_{m=1}^{n} \dot{\theta}_m)^2}{16E_g^m} \tag{A44}$$

$$= \frac{\dot{\varphi}_0^2}{16E_g^0} + \sum_{n=1}^{N} \frac{1}{16E_g^n}\left(\dot{\varphi}_0^2 + 2\dot{\varphi}_0 \sum_{m=1}^{n} \dot{\theta}_m\right.$$
$$\left. + \sum_{i=1}^{n}\sum_{j=1}^{n} \dot{\theta}_i\dot{\theta}_j\right) \tag{A45}$$

$$= \dot{\varphi}_0^2 \sum_{n=0}^{N} \frac{1}{16E_g^n} + 2\sum_{n=1}^{N}\sum_{m=1}^{n} \frac{\dot{\varphi}_0\dot{\theta}_m}{16E_g^n}$$
$$+ \sum_{n=1}^{N}\sum_{j=1}^{n}\sum_{i=1}^{n} \frac{\dot{\theta}_i\dot{\theta}_j}{16E_g^n} \tag{A46}$$

$$\mathcal{L}_c = \frac{\dot{\varphi}_0^2}{16E_c^1} + \frac{\dot{\varphi}_{-1}^2}{16}\left(\frac{1}{E_c^1} + \frac{1}{E_c^3}\right)$$
$$+ \frac{\dot{\varphi}_{-2}^2}{16}\left(\frac{1}{E_c^4} + \frac{1}{E_c^2}\right) + \frac{(\dot{\varphi}_0 + \sum_{m=1}^{N} \dot{\theta}_m)^2}{16E_c^2}$$
$$- \frac{\dot{\varphi}_0\dot{\varphi}_{-1}}{8E_c^1} - \frac{\dot{\varphi}_{-2}(\dot{\varphi}_0 + \sum_{m=1}^{N} \dot{\theta}_m)}{8E_c^2}$$
$$- \frac{\dot{\varphi}_{-2}eV}{8E_c^4} + \frac{\dot{\varphi}_{-1}eV}{8E_c^3} \tag{A47}$$

The term $\frac{(\dot{\varphi}_{-2})^2}{16E_c^4}$ will be added to the Lagrangian. The coupling constant for this case is,

$$\mathcal{L}_c = \frac{(\dot{\varphi}_{-1} - \dot{\varphi}_0)^2}{16E_c^1} + \frac{(\dot{\varphi}_{-1} - eV)^2}{16E_c^3} + \frac{(\dot{\varphi}_{-2})^2}{16E_c^4}, \tag{A48}$$

$$\mathcal{L} = \frac{\dot{\varphi}_+^2}{16E_c}\left(2 + \frac{NE_t}{E_g}\right) - \frac{\dot{\varphi}_+ eV}{4E_c}\left(\frac{3}{8} + \frac{E_t}{E_c}\right)$$
$$- \frac{NE_t}{16E_gE_c}\dot{\phi}eV - \frac{NE_t}{32E_gE_c}\dot{\phi}\dot{\varphi}_+ \tag{A49}$$
$$- \frac{E_t}{8E_gE_c}\sum_\mu \frac{c_\mu o_\mu}{\sqrt{2(N-1)}s_\mu^2}\dot{\xi}_\mu eV$$
$$- \frac{E_t}{8E_gE_c}\sum_\mu \frac{c_\mu o_\mu}{\sqrt{2(N-1)}s_\mu^2}\dot{\xi}_\mu\dot{\varphi}_+ + \mathcal{O}(e^2V^2) \tag{A50}$$
$$+ \left[(M_{00} + G_{00})\dot{\phi}^2 + 2\sum_\mu (M_{0\mu} + G_{0\mu})\dot{\phi}\dot{\xi}_\mu\right.$$
$$\left. + \sum_{\mu,\nu}(M_{\mu\nu} + G_{\mu\nu})\dot{\xi}_\mu\dot{\xi}_\nu\right] - \mathcal{U} \tag{A51}$$

a. Hamiltonian: All terms in the Hamiltonian (H_2) can be adopted via $N \to N-1$. If $C_g^N \neq C_g^1$ then this ground fluxonium and floating fluxonium have a larger difference in terms of frequencies of modes.

Appendix B: Undriven Fluxonium Circuit

In this appendix, we give the details of calculation and values (see Table V) of the measurement circuit in Fig. 2(a). The Hamiltonian for this circuit was derived in [26]. In addition, we also give some calculations post Hamiltonian derivation of the single-point connection circuits, shown in Fig. 11(b,c). For Hamiltonian derivations of these circuit, see Sec. A. Throughout the document we quote energies in units of h i.e. GHz. We assume,

- $N = 122$
- $C_g^0 = C_g^N \neq C_g^i \quad \forall i \in [1, 2, .., N-1]$.
- capacitance between the transmission line and readout resonator is infinite, such that the readout resonator is at voltage V.

General Fluxonium Circuit	Phase-Slip Junction	Josephson-Junction Array
Ground capacitance	$C_g^0 = C_g^N = 10 - 20 fF$	$\{C_g^1, ..., C_g^{N-1}\} = 0.05 - 0.1 fF$
Josephson Junction Energy	$E_{J_p} = 5 - 20$GHz	$E_{J_j} = 40 - 100$GHz
Capacitance Energy	$E_{C'} = 1 - 4$GHz	$E_{C_j} = 50 fF/115 E_{J_p}$GHz

Readout Circuit Parameters	Variables	Values
Readout Frequency	$\omega_r/2\pi$	6-9 GHz
Resonator kappa	κ_r	1-15MHz (easy to tune)
Readout Impedance	$Z(\omega)$	$100/\pi$ or $200/\pi$
qubit-R Coupling Capacitance (left)	$C_{c,1}$	1-2fF (Easy to tune)
qubit-R Coupling Capacitance (right)	$C_{c,2}$	1-2fF (Easy to tune)
qubit frequency	ω_{01}	33.7MHz
plasmon frequency	ω_{12}	6.082GHz
dispersive shift (readout resonator)	χ_R	0.5MHz for g=20MHz
Zero-point fluctuation of charge of resonator	$\phi_{r,ZPF}$	2.84
T_2* limitation from 50mK resonator	T_2	8.9ms
coupling coefficient	$g_{r,\phi}$	26.1MHz
dispersive shift	χ_{01}	0.38MHz
dispersive shift	χ_{12}	0.125MHz
self-kerr	K_r	0.001MHz (averaged upto 10 photons)

Parameters	Variables	Set 1
Number of junctions in the array	N	122
Phase-Slip JJ energy	E_{J_p}	7.3 GHz
Target capacitance	$e^2/2(C_g + C')$	1GHz
Phase-Slip junction capacitance+differential capacitance	$E_{C'}$	$(1 - 2/E_{g,p})^{-1}$GHz
JJA junction energy	E_{J_j}	60 GHz
JJA capacitance energy	E_{C_j}	0.74GHz
JJA ground capacitance	$E_{g,j}$	194 GHz
Phase-slip parasitic ground capacitance	$E_{g,p}$	1.94 GHz
Coupling capacitance	E_c	19.4 GHz
Readout loss rate	κ_r	1MHz
Readout Frequency	$\omega_r/2\pi$	8.5GHz
Quality-Factor	Q	8500
Zero-point fluctuation of charge operator	n_{ZPF}	1.4
Zero-point fluctuation of phase operator	ϕ_{ZPF}	0.357

TABLE V. Circuit Parameters. Capacitive energies E_g, E_c, etc.. are determined using $E_c = (e^2/2hC) = \frac{1.94e-5}{C} = 19.4/C(fF)$[GHz].

1. Circuit Features

- **Zero-point fluctuation of $e\hat{V}/h$:** We can use $eV = 2e^2(n_r/\sqrt{2})/C_r = 4E_{C_r}(n_r/\sqrt{2})$. If we absorb the factor of $4E_{C_r}$ in the coupling coefficient, then $\frac{n_{ZPF}}{\sqrt{2}} = \left(\frac{E_L}{8E_{C_r}}\right)^{1/4}$ and $e\hat{V} = 4E_{C_r}\hat{n}$. This is exactly equal to the quantity in Table V [43].

- **Zero-point fluctuation of $n_{\phi,r}$:** For the qubit mode, we use the harmonic oscillator approximation where we define, $\frac{n_{ZPF}}{\sqrt{2}} = \left(\frac{E_J^j}{8N\tilde{E}_C^\phi}\right)^{1/4} = 1/\phi_{ZPF} \approx 0.36(H_1), 0.34(H_2), 0.34(H_3)$. This approximation holds correct if the convergence is taken care of using proper cutoff on this basis.

- **Zero-point fluctuation of $n_{\mu,r}$:** For parasitic modes, it is $n_{ZPF} = \left(\frac{E_J^j}{8E_{C,\mu}^c}\right)^{1/4}$. We could use this to compute the absolute strengths for parasitic modes and resonator couplings.

- **Occupation Number of the Parasitic**

Modes: As discussed in the main text, the parasitic mode frequencies are given by,

$$\omega_\mu^o = \sqrt{8E_{c,\mu}^o E_{J_j}} \tag{B1}$$

$$\omega_\mu^e = \sqrt{8E_{c,\mu}^e E_{J_j}} \tag{B2}$$

Here we have expressed ω for the case when energies are expressed in GHz. The thermal population of the parasitic modes can be calculated as $n = \frac{1}{e^{hf/kT}-1}$ where k, T, f are the Boltzmann constant, temperature, and mode frequency, respectively. The frequency curve shown in Fig. 2 saturates at 18.8 GHz while the occupation number of the lowest even (odd) mode stands at 12.06 (7.25). Only the even modes couple to the readout and parasitic modes. The occupation number of the first even (odd) mode is $9.3e - 6$ $(9e - 4)$. The highest mode saturates at an occupation number of $1.4e - 8$. Importantly, For a temperature of $20mK$, the lowest odd mode population is down to $6.3e - 8$.

1. Total ground capacitance.

(a) $H_1 : E_t = (\frac{N-1}{E_g} + \frac{2}{E_{g1}} + \frac{2}{E_c})^{-1} = 0.57\text{GHz}$

(b) $H_2 : E_t = (\frac{N-1}{E_{g_j}} + \frac{2}{E_{g_p}} + \frac{1}{E_c})^{-1}$

(c) $H_3 : E_t = (\frac{N-1}{E_{g_j}} + \frac{1}{E_{g_p}} + \frac{1}{E_c})^{-1}$

2. Qubit Charging energy ($4E_c^\phi \hat{N}_\phi^2$).

(a) H_1 : $\bar{E}_c^\phi = (\frac{1}{4E_t}\left(1 - \frac{2}{3}\frac{(N+1)(N-1)}{N}\frac{E_t}{E_g}\right) + \frac{1}{E_{C'}} + \frac{1}{NE_{C_j}})^{-1} = 0.92$ GHz.

(b) H_2 : $\bar{E}_c^\phi = (\frac{1}{4E_t}\left(1 - \frac{E_t}{E_c}\right)^2\left[1 - \frac{2}{3}\frac{N-1}{N}\right] + \frac{1}{E_{C_p}} + \frac{1}{NE_{C_j}})^{-1}$.

(c) H_3 : $\bar{E}_c^\phi = (\frac{1}{4E_t}\left(1 - \frac{E_t}{E_c}\right)^2\left[1 - \frac{2}{3}\frac{N-2}{N-1}\right] + \frac{1}{E_{C_p}} + \frac{1}{NE_{C_j}})^{-1}$.

3. Even Parasitic Mode Charging Energy ($4E_{c,\mu}^e \hat{N}_\mu^2$).

(a) $H_1 : \tilde{E}_{c,\mu}^e = (\frac{1}{E_{C_j}} + \frac{1}{4E_g s_\mu^2})^{-1}$

(b) H_2 : Same as H_1

(c) H_3 : Same as H_1

4. Qubit-Readout Coupling ($g_{\phi r}\hat{N}_\phi \hat{N}_\mu$).

(a) $H_1 : \frac{\tilde{E}_c^\phi}{E_c}$

(b) $H_2 : \frac{\bar{E}_c^\phi}{E_c}\left[\frac{(N+1)E_t}{2E_{g_j}} + \frac{E_t^2 \tilde{E}_{c,\mu}^o}{8E_{g_j}^2 E_c}\left(\frac{c_\mu^2}{2N s_\mu^4}\right)\right]$

(c) $H_3 : \frac{\bar{E}_c^\phi}{E_c}\left[\frac{NE_t}{2E_{g_j}} + \frac{E_t^2 \tilde{E}_{c,\mu}^o}{8E_{g_j}^2 E_c}\left(\frac{c_\mu^2}{2(N-1)s_\mu^4}\right)\right]$

5. Qubit-Parasitic Coupling ($g_{\phi\mu}\hat{N}_\phi \hat{N}_\mu$)

(a) $H_1 : \sqrt{\frac{2}{N}}\frac{\tilde{E}_c^\phi \tilde{E}_{c,\mu}^e c_\mu}{E_{g_j}s_\mu^2}$

(b) $H_2 : \sqrt{\frac{2}{N}}\frac{\bar{E}_c^\phi \tilde{E}_{c,\mu}^e c_\mu}{E_{g_j}s_\mu^2}$

(c) $H_3 : \sqrt{\frac{2}{N-1}}\frac{\bar{E}_c^\phi \tilde{E}_{c,\mu}^e c_\mu}{E_{g_j}s_\mu^2}$

6. Readout-Parasitic Coupling ($g_{\mu r}\hat{N}_\mu \hat{N}_r$)

(a) $H_1 : \frac{\tilde{E}_c^\phi \tilde{E}_{c,\mu}^e c_\mu}{4\sqrt{2N}E_{g_j}E_c s_\mu^2}$

(b) $H_2 : \frac{\bar{E}_c^\phi \tilde{E}_{c,\mu}^e c_\mu}{4\sqrt{2N}E_{g_j}s_\mu^2 E_c}\left[\frac{(N+1)E_t}{2E_g}\right]$

(c) $H_3 : \frac{\bar{E}_c^\phi \tilde{E}_{c,\mu}^e c_\mu}{4\sqrt{2(N-1)}E_{g_j}s_\mu^2 E_c}\left[\frac{NE_t}{2E_{g_j}}\right]$

2. Qubit Hamiltonian

The qubit Hamiltonian H_ϕ is diagonalized in the Fock state basis, where we have used $\hat{x} = x_{zpf}(a + a^\dagger)$ and $\hat{p} = -ip_{zpf}(a - a^\dagger)$, then $x_{zpf} = \frac{1}{2p_{zpf}}$. Each zero-point fluctuation value in the two cases is related as $ZPF_2 = ZPF_1/\sqrt{2}$.

a. *Energy Spectrum for H_1:* The Hamiltonian of the qubit subspace is $H_\phi = 4\tilde{E}_C^\phi n_\phi^2 + E_{J,p}\cos\phi + \frac{1}{2}E_L\phi^2$, where $E_L = \frac{E_J^a}{N}$. The zero-point fluctuation of the unit-less phase operator ϕ is $n_{ZPF,\phi}^{-1} = 1.39$.

b. *Charge Matrix Elements for H_1, H_2, H_3:* Here, using the approximations described in the appendix, we get the following charge matrix elements for the qubit subspace.
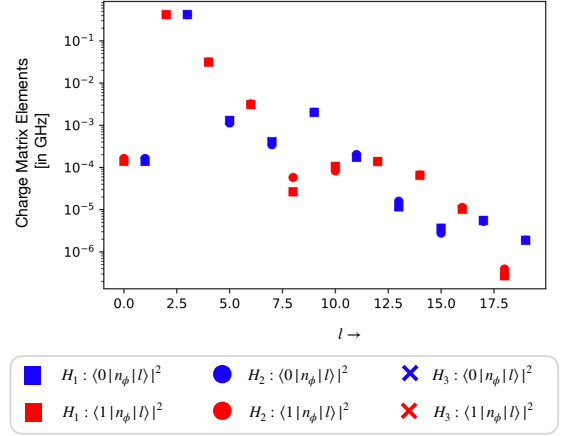

FIG. 12. Charge Matrix Elements (squared) for all three circuits. Note that in the equations below we substitute $\langle l|n|l'\rangle = in_{ZPF}\langle l|a - a^\dagger|l'\rangle$ where $n_{ZPF} = \frac{1}{\sqrt{2}}\left(E_{J,j}/8NE_C\right)^{1/4}$. The charge matrix elements between odd-odd or even-even is zero (points not seen in log plot) due to the symmetry of cosine potential at $\varphi_{ext} = 0.5\Phi_0$, where Φ_0 is the flux quantum.

c. *Coupling Constant Landscape:* The coupling constants decrease with increasing μ. We plot the coupling constants for the parallel circuit named H_1 in Fig. 2 of the main text in Fig. 13. In addition, we give coupling constants of the single-point connection circuits, elaborated in Sec. A.
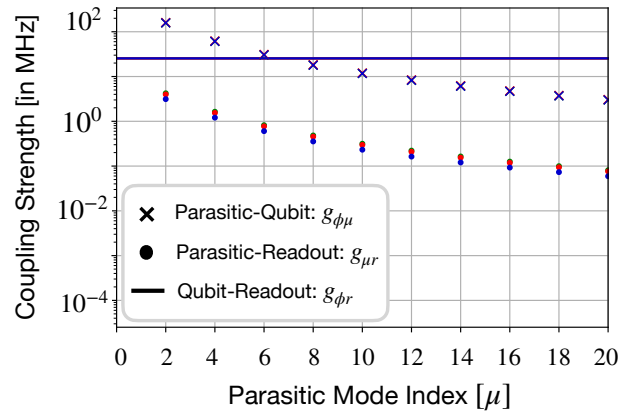
FIG. 13. Absolute values of the coupling strengths in GHz for various circuits. H_1 (green): Parallel circuit (see Fig. 2), H_2 (blue): single-Point connection with floating fluxonium (see Fig. 11 (b)), and H_3 (red): single-Point Connection with grounded fluxonium (see Fig. 11 (c)). The behavior for all circuits is the same, thus the discussion in the main text focused on H_1 can be easily extended to H_2, H_3. Coupling to odd parasitic modes is zero due to the symmetries of the circuit [26].

Below in Fig. 14 is the dependence of charging energies and coupling constants on the number of junctions as well as the ground capacitance.

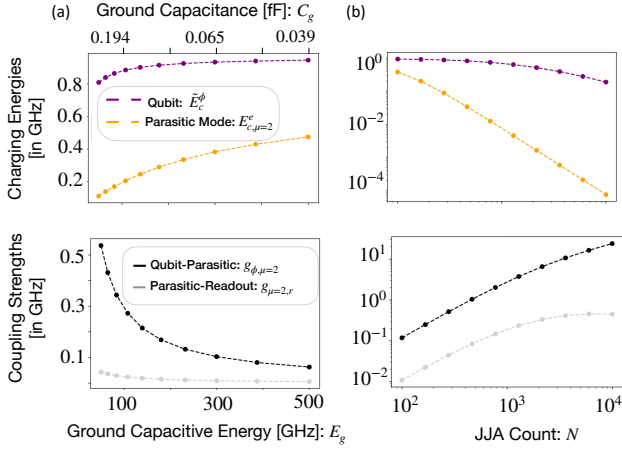FIG. 14. The qubit charging energy in (a) decides the frequency and the parasitic charging energy in (b) decides the parasitic mode frequency. (c,d) give the plots for the coupling strengths of the parasitic mode to readout and qubit, respectively. All plots are obtained under linear JJA approximation. [SS: Add factor $1/2\pi$ for the coupling strengths notations in the legend. Correct these plots]

3. Dispersive Hamiltonian

We use the Schrieffer-Wolff approximation to extract the readout parameters in Table. II, for example, dispersive shift of the qubit due to the parasitic modes $\chi_{\phi\mu}$ and the readout mode $\chi_{\phi r}$ [26] used to generate Fig. 6,

$$2\pi H = \frac{\omega_q}{2}\sigma_z + \sum_\mu (\omega_\mu + k_\mu) a_\mu^\dagger a_\mu + \omega_r a_r^\dagger a_r$$
$$+ \chi_{r,\phi}\sigma_z a_r^\dagger a_r + \sum_\mu \chi_{\mu,\phi}\sigma_z a_\mu^\dagger a_\mu$$
$$+ \sum_\mu \chi_{r\mu} a_\mu^\dagger a_\mu a_r^\dagger a_r \qquad (B3)$$
$$= \frac{\omega_q}{2}\sigma_z + \left(\omega_r + \chi_{r\phi}\sigma_z\right) a_r^\dagger a_r$$
$$+ \sum_\mu \left(\omega_\mu + k_\mu + \chi_{r\mu}a_r^\dagger a_r + \chi_{\mu\phi}\sigma_z\right) a_\mu^\dagger a_\mu \qquad (B4)$$

where ω_q or $\omega_{01} = \epsilon_0 - \epsilon_1$

$$+ |\langle 0|p_\phi|1\rangle|^2 \left[16g_{r\phi}^2 E_{C_r}^2 \sqrt{\frac{E_{L_r}}{32E_{C_r}}}\frac{2\epsilon_{01}}{\epsilon_{01}^2 - \omega_r^2} \right.$$
$$\left. + \sum_\mu \left\{ g_{\mu\phi}^2 \sqrt{\frac{E_J^j}{32\tilde{E}_{C,\mu}^e}}\frac{2\epsilon_{01}}{\epsilon_{01}^2 - \omega_\mu^2} \right\} \right]$$
$$+ \sum_{l>1} 16g_{r\phi}^2 E_{C_r}^2 \sqrt{\frac{E_{L_r}}{32E_{C_r}}} \left[\frac{|\langle 0|p_\phi|l\rangle|^2}{\epsilon_{0l} - \omega_r} \right.$$
$$\left. - \frac{|\langle 1|p_\phi|l\rangle|^2}{\epsilon_{1l} - \omega_r} \right] + \sum_{l>1,\mu} \left\{ g_{\mu\phi}^2 \sqrt{\frac{E_J^j}{32\tilde{E}_{C,\mu}^e}} \times \right.$$
$$\left. \left[\frac{|\langle 0|p_\phi|l\rangle|^2}{\epsilon_{0l} - \omega_\mu} - \frac{|\langle 1|p_\phi|l\rangle|^2}{\epsilon_{1l} - \omega_\mu} \right] \right\} \qquad (B5)$$

$$k_{\mu\in 2\mathbb{Z}} = 16E_{C_r}^2 \sqrt{\frac{E_{L_r}}{32E_{C_r}}}\sqrt{\frac{E_J^j}{32E_C^e}}\left[\frac{g_{r\mu}^2}{\omega_\mu - \omega_r}\right]$$
$$\leq \mathcal{O}(10^{-8}) \qquad (B6)$$

$$\chi_{r,\phi} = 16g_{r\phi}^2 E_{C_r}^2 \sqrt{\frac{E_{L_r}}{32E_{C_r}}}\frac{2\epsilon_{01}}{\epsilon_{01}^2 - \omega_r^2}|\langle 0|p_\phi|1\rangle|^2$$
$$+ 16g_{r\phi}^2 E_{C_r}^2 \sqrt{\frac{E_{L_r}}{32E_{C_r}}}\left[\sum_l |\langle 0|p_\phi|l\rangle|^2 \frac{\epsilon_{0l}}{\epsilon_{0l}^2 - \omega_r^2} \right.$$
$$\left. - \sum_l |\langle 1|p_\phi|l\rangle|^2 \frac{\epsilon_{1l}}{\epsilon_{1l}^2 - \omega_r^2} \right] \qquad (B7)$$

$$\chi_{\mu,\phi} = g_{\mu\phi}^2 \sqrt{\frac{E_J^j}{32\tilde{E}_{C,\mu}^e}}\frac{2\epsilon_{01}}{\epsilon_{01}^2 - \omega_\mu^2}|\langle 0|p_\phi|1\rangle|^2$$
$$+ g_{\mu\phi}^2 \sqrt{\frac{E_J^j}{32\tilde{E}_{C,\mu}^e}}\left[\sum_l |\langle 0|p_\phi|l\rangle|^2 \frac{\epsilon_{0l}}{\epsilon_{0l}^2 - \omega_\mu^2} \right.$$
$$\left. - \sum_l |\langle 1|p_\phi|l\rangle|^2 \frac{\epsilon_{1l}}{\epsilon_{1l}^2 - \omega_\mu^2} \right] \quad \text{(see Fig. 15)} \qquad (B8)$$

Therefore $\omega_q = -7e - 04$ GHz, $\omega_{q,r} = -1.1e - 03$ GHz, see Fig. 15 for $\omega_{q,\mu}, \chi_{\mu,\phi}$.

The dispersive shift between the qubit and the readout is small due to the small charge matrix elements. The primary element which contributes to this quantity is the 03 and 12 charge matrix elements.
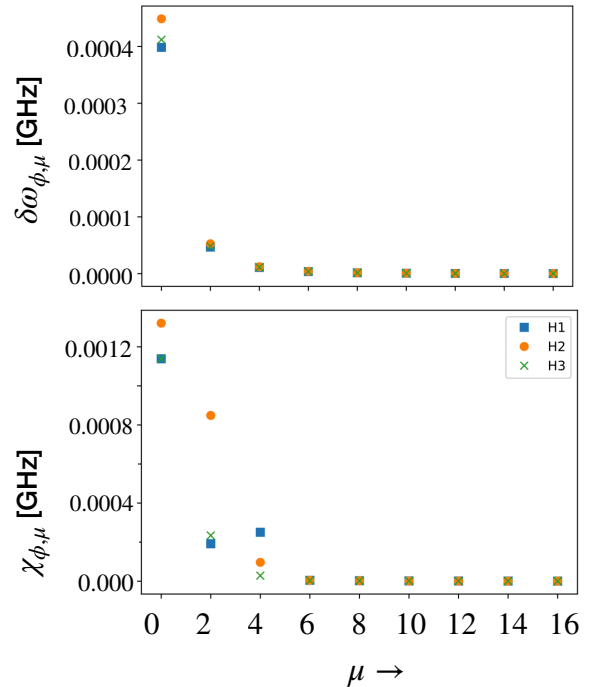

FIG. 15. All values are in $\frac{GHz}{2\pi}$ units. The color code follows: H_1 (blue), H_2 (orange), H_3 (green) for the three circuits shown in Fig. 14(a-c). (Top) Change in the qubit frequency due to parasitic mode μ (Bottom) Dispersive shift χ_μ of the qubit concerning the parasitic mode μ.

Appendix C: Driven Fluxonium Circuit

Here, we will discuss the several analyses used in the driven fluxonium circuit including the semi-classical approximation and methods used in Sec. III to compute the readout efficiency. We first start with the derivation of $H_{s.c.}$ in Eq. 6. Derivation goes here

1. Approximations for Numerical Modelling

We use the following three approximations to make the problem at hand simpler

- Restriction to $\mu = 2$. We restrict our analyses to the closest even parasitic mode that couples most strongly to the qubit and the readout as evident from Fig. 14(d). This assumption helps us to lower bound the errors. Although it will be an interesting study to see if there are transitions caused due to higher modes that are more probable but in this work we aim at a proof of principle quantitative evidence of the presence of such transitions even with out modest assumptions.

- Semi-classical drive approximation. This approximation treats the readout resonator classically as described in Refs. [18–21] reducing one mode from our numerical simulation. This assumption is essential since unlike the case of transmon or fluxonium without collective modes, with all the above approximation, a full quantum simulation of the problem will still require three modes.

- Linear JJA Approximation. We assume that the parasitic modes behave as linear oscillators due to the large $E_{J_j}/E_{C_j} = 200$ ratio. This approximation is explained in App. B. The nonlinear corrections to our results, while essential, is beyond the scope of this work. For details on how nonlinear corrections affect different circuit parameters in play we direct the readers to Ref. [26]. Due to this assumption, we can use a Hilbert size of 20×3 where only three levels are assumed in the linear parasitic mode subspace. In the presence of nonlinearity, the Hilbert size would need to be much larger to capture the required effects. Note that for the conclusions drawn in this paper, we are only interested in the presence of p-MIST processes and do not claim to quantify how many such transitions can be present. Hence, 3 levels in the parasitic mode are enough. In addition, we have verified that changing the truncation of the parasitic mode to 10 levels does not change the energy spacing.

Here goes the truncation figure

2. Stark Shift

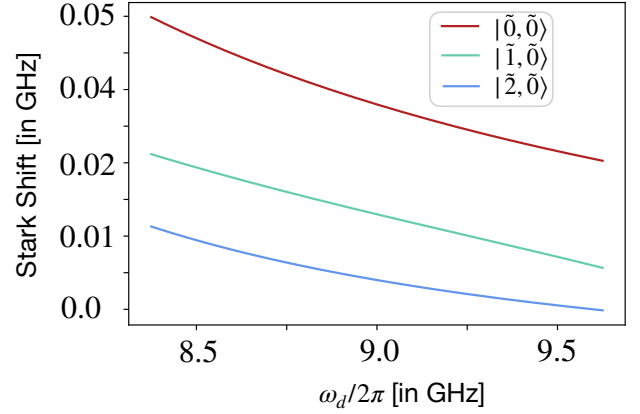To observe a state transition the primary requirements are high charge matrix elements and low en-

FIG. 16. Stark shift in different qubit levels under observation for readout computed using Eq. C1.

ergy difference. The eigen-eniergies of the states in question are changed with an increase in the number of readout photons or, in this case, the drive strength. So, in this section, we compute the stark shifted eigen-energies which can help in the prediction of an avoided crossing, given $\bar{n}_r, \omega_r$ and the charge matrix elements. These stark shift formulas are used in the computing the probability of transitions using generalized Fermi's golden rule and Landau-Zener calculations. Let $|i\rangle$ be a state in the eigenspace of $H_{int} = H_\phi + H_{\mu=2} + g_{\phi\mu}\hat{N}_\phi\hat{N}_\mu$. Following derivations in App. B the ac stark-shift in the energy of state $|i\rangle$ at an average number of readout photons $\bar{n}_r$ is given by,

$$\chi_i(\bar{n}_r) = 2\bar{n}_r \sum_f \omega_{if} \left[\frac{g_{\phi r}|\langle i|\hat{N}_\phi|f\rangle|^2}{\omega_d^2 - \omega_{if}^2} + \frac{g_{\mu r}|\langle i|\hat{N}_\mu|f\rangle|^2}{\omega_d^2 - \omega_{if}^2} \right]$$
(C1)

Here $\omega_{if} = E_f - E_i$ denote the energy difference in the eigen-energies of the $|i\rangle$. The impact due to the second term as expected is much smaller than the first term, and hence $g_{\phi r}$ primarily governs this stark shift.

3. Transition Rates and Quasienergies

Below we guess process responsible for each transition using first and second order fermi's golden rule calculations. We have computed rates using fermi's golden rule up to second order terms, as many of these transitions occur between a parity-conserving states, a forbidden first order transition. We compute these transitions involving up to 4 readout photons, as suggested by energy conservation. Under the same classical approximation, we can identify our parent Hamiltonian as H_0 and perturbation V as follows,

$$H_0 = H_\phi + \omega_\mu \hat{a}_\mu^\dagger \hat{a}_\mu + g_{\phi,\mu}\hat{N}_\phi\hat{N}_\mu \qquad (C2)$$

$$V = 2\sqrt{\bar{n}_r}(g_{r,\phi}\hat{N}_\phi + g_{r,\mu}\hat{N}_\mu)\sin\omega_d t, \qquad (C3)$$

whereμ is the density of states which will be a Dirac Delta function in the absence of loss while it will be

Lorentzian in the presence of loss $\frac{\kappa}{2\pi} = 50$. In units of $\hbar$ we have,

$$\Gamma_{i \to f} = |\langle f|H_1|i\rangle|^2 \mu(E_i - E_f) \quad \text{(first-order)} \quad \text{(C4)}$$

$$= \sum_m \frac{|\langle f|H_1|m\rangle \langle m|H_1|i\rangle|^2}{|E_i - E_m - k\hbar\omega_d|^2} \mu(E_f - E_i - n\hbar\omega_d)$$

$$\text{(second-order)} \quad \text{(C5)}$$

We use a Lorentzian density of states at a $\frac{\kappa}{2\pi} = 1.5$ KHz. Here $k < n$ is used to compute the detuning with the intermediate state involved in the transition. Note that increasing the width of the Lorentzian κ resulting in an increase in the FG rates. Thus, here the decay rate does not yield any insights into the diabaticity at the transition, and hence the κ variation here is not the same as the κ variation in Sec. III B.

While these calculations include stark shifts in the energies of the states, we know that the first-order perturbative correction is not enough for some of the more higher states as seen in the comparisons of quasi-energies from Floquet simulations and predicitions of stark shifted transitions. Thus, the computation below is only based on a heuristic developed from this approximate calculation. All transitions are computed at $\bar{n}_r = 50$. We note that the fermi's golden rule calculations higher rates at the frequencies predicted by $g_{\phi\mu} = 0$ case where the two frequencies are extremely different, for example, transitions 10 and 14. This happens since the Fermi's golden rule calculations are only approximately computing the stark-shifted energies for states which are more hybridized due to the presence of coupling $g_{\phi\mu}$. This behaviour is evident in Figs. 17, 18, 19. We will compare the considerable FG rates with well-separated quasi-energy gap at the avoided crossings Δ_{ac} seen in these figures.

For the case of $|i\rangle = |\tilde{0}, \tilde{0}\rangle$ shown in Fig. 17, we quote the rates for each process and state how many readout photons were involved, guess the possible intermediate state and whether it could be a first- or second-order process. This heuristic analysis is still interesting since it helps us understand the processes involved behind general MIST processes and p-MIST processes, identifying any unique feature or extremely high rates, if so.

1. This is a first order transition involving three readout photons ($3r$) which yields a fermi's golden rule rate of 40 KHz.

2. The first process is a second-order process which absorbs two photons ($2r$) through an intermediate state with energy close to $E_i + \omega_r$ at a rate of 4 MHz where $\Delta_{ac} = 4$ MHz. The second process is a second-order which absorbs four photons ($4r$) through an intermediate state close to $E_i + 3\omega_r$ at a rate of 22 KHz.

3. This is a Rabi transition involving a virtual state via a second-order two-photon process ($2r$) at a rate of $0.028 KHz$.

4-6. The first transition is a second order two-photon process $2r$ with an FG rate of 1.26 KHz at $\omega_r = 9.36$ GHz. The second process is a Rabi transition at a rate of 10 KHz.

Next, we look at the transition rates for the $|\tilde{0}, \tilde{1}\rangle$, the state involved in the computation as well as readout in a low-frequency fluxonium, shown in Fig. 18.

7. This is a second order process involving four readout photons ($4r$) at a rate of 21 KHz. The intermediate state involed is close to a frequency of $E_i + 3\omega_r$.

8. This is a second order process involving two readout photons ($2r$) with a transition rate of 45 KHz. The energy gap at the avoided crossing for this transition is less than 1 MHz.

9. This is a second order process involving four readout $4r$ photons occurring at a rate of 0.95 KHz, where the intermediate state energy is close to $E_i + 3\omega_r$.

10. This is a second order process involving two readout $2r$ photons occurring at a rate of 91 KHz. Fig. 5 also confirms that the transition 9 occurs with a higher probability compared to transition 8. The energy gap at the avoided crossing is

11. This is a first order process involving three readout photons ($3r$) occurring at a rate of 2.2 KHz.

12. This is a second order process involving two readout photons ($2r$) occurring at a rate of 52 KHz where $\Delta_{ac} = 1.1$ MHz.

Finally, we look at the transition rates for the $|\tilde{0}, \tilde{2}\rangle$, the state involved in the readout of a low-frequency fluxonium, shown in Fig. 19.

13. This is a second order process involving two-readout photons ($2r$) occurring at a rate of 16 (1) MHz which is the same as Δ_{ac}.

14. This is a second order process involving two-readout photons ($2r$) occurring at a rate of 2.2 KHz.

15. The first process is first order while the second process is second order, both involving ($1r$) and ($2r$) readout photons. The rates of these transitions are 1.48 KHz and 28 KHz, respectively. The energy gap at this avoided crossing is 4 MHz. Thus, this transition appears to be a either a higher order process or a weaker transition.

4. Landau-Zener Probabilities

We compute the Landau-Zener probabilties numerically using the quasienergies from the Floquet simulations and analytically using the stark-shifted eigenenergies. In order to convert the Floquet simulation used with variation in $\bar{n}_r$ at a fixed time t (ignoring the short scale fast dynamics over a time period), in this case, we will use a time-dependent case where $\bar{n}_r$ varies as $\bar{n}_r = 50(1 - e^{-\kappa T/2})^2$ to emulate change in

FIG. 17. MIST processes from Table III involving the $|\tilde{0}, \tilde{0}\rangle$ state. (Top row) Fluxonium subspace $\langle n_\phi \rangle$. (Middle) Parasitic mode subspace $\langle n_\mu \rangle$ (Bottom) Stark-shifted eigen-energies (dashed) and quasi-energies (solid) from Floquet simulations, corresponding to the initial state i as per the legend. Inset shows avoided crossing of quasi-energies. Floquet results are extracted from numerical data used for Fig. 3.
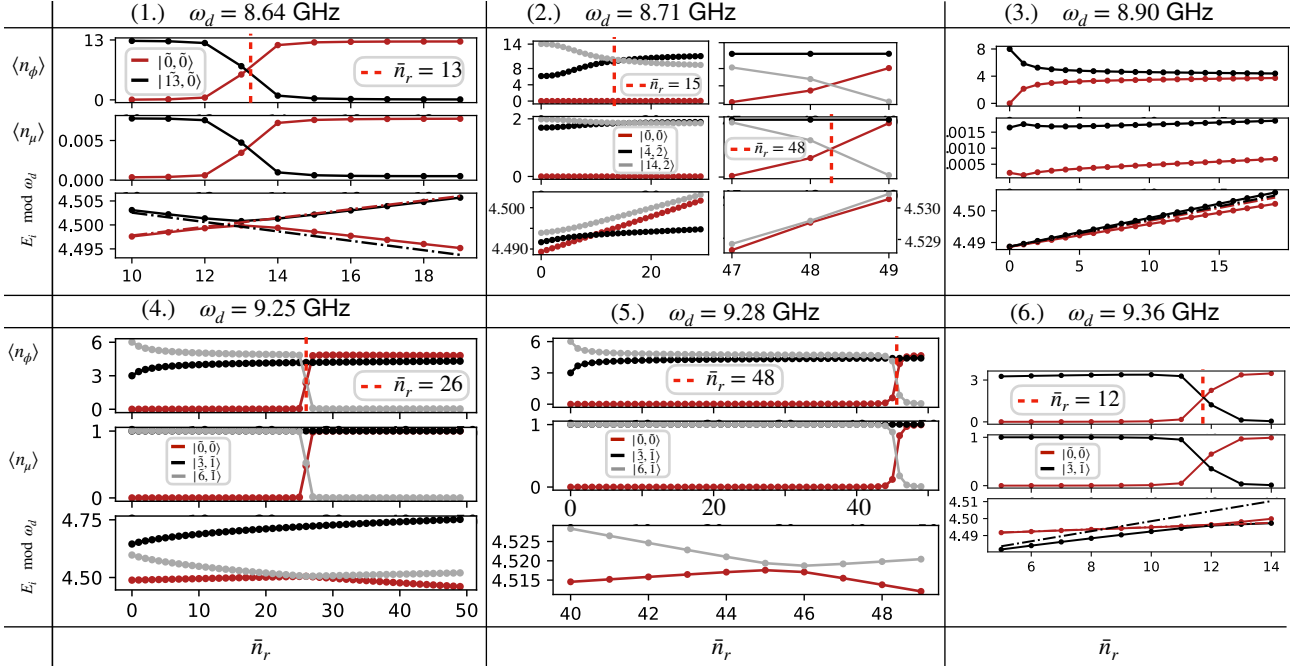

FIG. 18. MIST processes from Table III involving the $|\tilde{1}, \tilde{0}\rangle$ state. (Top row) Fluxonium subspace $\langle n_\phi \rangle$. (Middle) Parasitic mode subspace $\langle n_\mu \rangle$ (Bottom) Stark-shifted eigen-energies (dashed) and quasi-energies (solid) from Floquet simulations, corresponding to the initial state i as per the legend. Inset shows avoided crossing of quasi-energies. Floquet results are extracted from numerical data used for Fig. 3.

readout photons from dissipation. The numerical calculations use the probability for Landau-Zener transitions given in [29] for an avoided crossing observed

between states i, f,

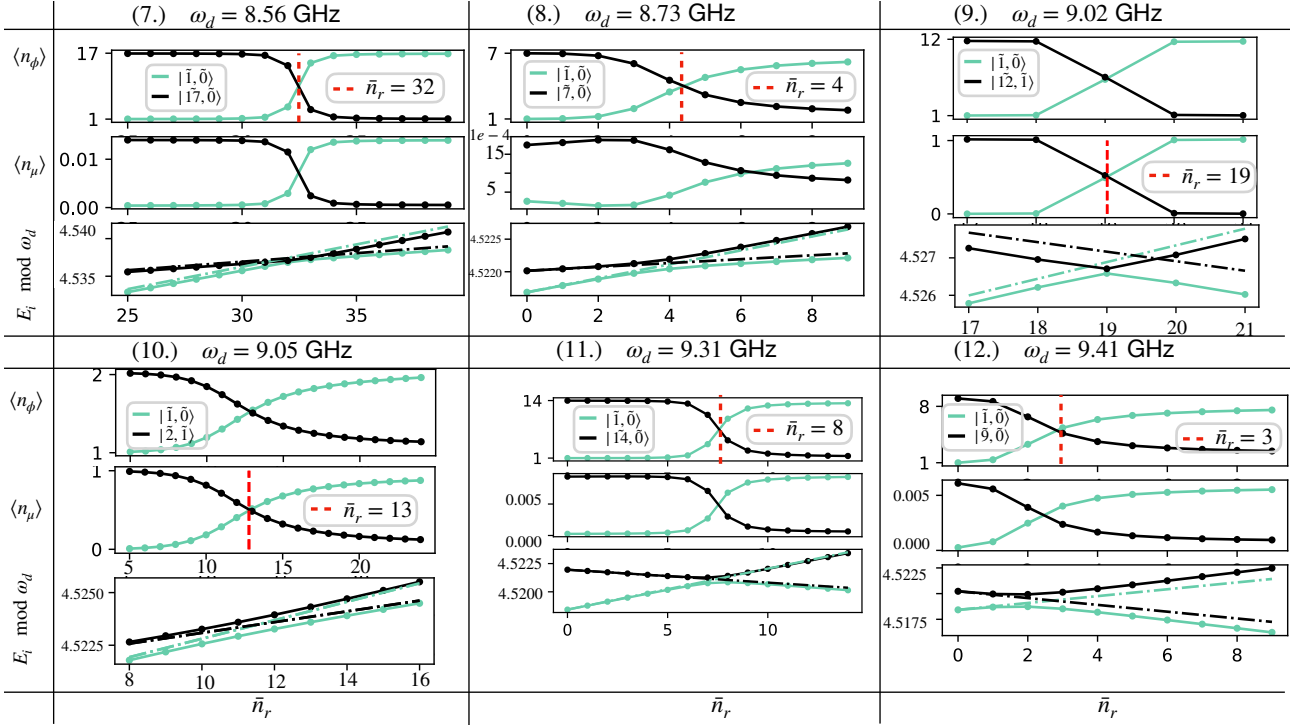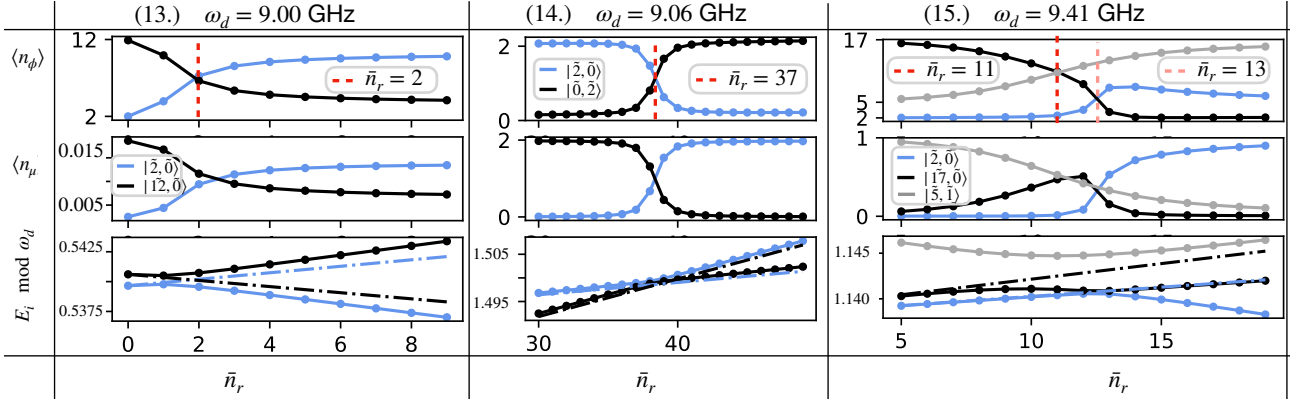$$P_{LZ} = \exp\left[-\pi \frac{\Delta_{ac}^2}{2v}\right], \tag{C6}$$

FIG. 19. MIST processes from Table III involving the $|\tilde{2}, \tilde{0}\rangle$ state. (Top row) Fluxonium subspace $\langle n_\phi \rangle$. (Middle) Parasitic mode subspace $\langle n_\mu \rangle$ (Bottom) Stark-shifted eigen-energies (dashed) and quasi-energies (solid) from Floquet simulations, corresponding to the initial state i as per the legend. Inset shows avoided crossing of quasi-energies. Floquet results are extracted from numerical data used for Fig. 3.

$$\text{where } v = \sqrt{2\Delta_{ac}\left|\frac{d^2\epsilon_f}{d\bar{n}_r(t)^2}\right|_{t_{ac}}\frac{d\bar{n}_r(t)}{dt}\Big|_{t_{ac}}} \quad \text{(C7)}$$

Here, the variable ϵ_j is the numerically computed quasi-energy obtained from Floquet simulations, while Δ_{ac} refers to the quasi-energy difference at avoided crossing.

For the analytical calculations, we use the well-known formula (with energy in units of GHz),

$$P_{LZ} = \exp\left[-4\pi^2 \frac{V}{\frac{\partial \omega_{if}}{\partial \bar{n}_r(t)}\frac{d\bar{n}_r(t)}{dt}}\right], \quad \text{(C8)}$$

$$\text{where} \quad V = |\langle i|H_t|f\rangle|^2 \quad \text{(C9)}$$

$$\omega_{if} = E_f + \chi_f(\bar{n}_r(t)) - E_i - \chi_i(\bar{n}_r(t)) \quad \text{(C10)}$$

Here $\chi_i(\bar{n}_r(t)), \chi_f(\bar{n}_r(t))$ are ac stark shifts in the eigen-energies of i, j due to $\bar{n}_r$ average readout photons. See app. C 2 for the calculation of these quantities.

5. Parasitic Dephasing due to Thermal Effects

In this appendix, we lay out in detail our calculations of dephasing induced by the random occupation of the parasitic modes due to thermal effects. We assume a scenario where the circuit is connected to a bath at $0K$ such that thermal photons can be set to $n_{th} = 0$. The parasitic mode is randomly populated to some non-zero $\bar{n}_\mu$ induced by the coupling of the readout with the parasitic mode. Now, at some point this population will go back to $\bar{n}_\mu = 0$ due to the decay of the parasitic modes dominated by the rate $\kappa_\mu = \frac{\omega_\mu}{Q_\mu}$. Here Q_μ, ω_μ are the quality factor and frequency of the parasitic mode. We are set to compute the dephasing due to the fluctuation in this quantity as the parasitic mode decays. We can compute the total decay rate of the parasitic modes as follows [44],

$$k_\mu = \kappa_r \frac{g_{\mu,r}^2}{\Delta^2} + \frac{\omega_\mu}{Q_\mu}, \quad \text{(C11)}$$

where Δ is the detuning between the parasitic mode frequency and the readout drive frequency. The first

terms and second terms depict contributions from Purcell effect due to the readout resonator ($\approx$ Hz) and the quality factor Q_μ of the parasitic modes ($\approx$ KHz-MHz). The second term dominates the expression and will determine the decay rate of the parasitic modes.

In this context, we use the methods described in Ref. [45] to compute the dephasing of a qubit given the initial occupation of the parasitic mode and the strong coupling between the qubit and the parasitic mode. Here, we use the dispersive Hamiltonian (see Eq. B4) of qubit-parasitic mode system, without the readout. This assumption on the system is well-suited to cases where measurement has populated the parasitic mode. In the absence of any state transition in the fluxonium circuit, the parasitic mode is populated to $\bar{n}_\mu = \mathcal{O}(10^{-4})$ as shown in Fig. 7(a) due to the readout-parasitic mode coupling.

$$\frac{H}{\hbar} = \frac{\omega_q}{2}\sigma_z + \sum_\mu \left(\omega_\mu + k_\mu + \chi_{\mu\phi}\sigma_z\right)a_\mu^\dagger a_\mu, \quad \text{(C12)}$$

$$+ \xi_{\mu r}\hat{N}_\phi \sin \omega_d t \quad \text{(C13)}$$

where, κ_μ is the lamb shift, χ_μ is the stark shift, and ω_μ is the frequency of the parasitic mode. The variable ω_q denotes the qubit frequency i.e. the energy gap between the ground and the first excited state of the qubit potential. We ignore the qubit drive in this case since it will not play a role in the question of concern. In the presence of a qubit coupling, the state transitions will dominate the lifetimes and thus calculation of dephasing rates takes a backseat. In this scenario we are in the weak damping, strong coupling limit as $g_{\mu\phi}$ is of the order of GHz while the damping $\kappa_\mu = \frac{\omega_\mu}{Q_\mu}$ is of the order of MHz or KHz since all parasitic modes are designed to be high Q cavities. In the limit of zero temperature Ref. [45] shows that the dephasing rate coincides with what has been found in Ref. [44]. We use the calculations for the dispersive Hamiltonian (see Eq. B4 in App. B) to calculate for the drive-dependent dephasing rate at zero temperature quoted in [44, 45] assuming an initial $\bar{n}_r$.

$$\Gamma_\theta = \sum_\mu \frac{1}{2} \frac{|\xi_{\mu,r}|^2 \chi_{\mu,\phi}^2 \kappa_\mu}{[(\Delta + \chi_{\mu,\phi})^2 + (\kappa_\mu/2)^2]}$$

$$\times \frac{1}{[(\Delta - \chi_{\mu,\phi})^2 + (\kappa_\mu/2)^2]} \qquad \text{(C14)}$$

$$= \sum_\mu \left[\frac{\chi_{\mu,\phi}^2 \kappa_\mu}{\Delta^2 + \kappa^2/4 + \chi_{\mu,\phi}^2} \right] \bar{n}_\mu, \qquad \text{(C15)}$$

The thermal population of the parasitic modes is capped at 10^{-3} for $T = 50 mK$ (see App. B) inducing a dephasing rate of $\Gamma_\phi = 10^{-6}$ GHz.

Appendix D: Alternative Circuit

Here goes the details on Will Oliver's parameters and figures for coupling strengths etc.

[1] Phys. Rev. X 9, 041041 (2019) - High-Coherence Fluxonium Qubit (2019).

[2] A. Somoroff, Q. Ficheux, R. A. Mencia, H. Xiong, R. Kuzmin, and V. E. Manucharyan, Millisecond Coherence in a Superconducting Qubit, Physical Review Letters 130, 267001 (2023), publisher: American Physical Society.

[3] Fluxonium: Single Cooper-Pair Circuit Free of Charge Offsets | Science (2009).

[4] N. Earnest, S. Chakram, Y. Lu, N. Irons, R. K. Naik, N. Leung, L. Ocola, D. A. Czaplewski, B. Baker, J. Lawrence, J. Koch, and D. I. Schuster, Realization of a $\mathrm{\ensuremath{\Lambda}}$ System with Metastable States of a Capacitively Shunted Fluxonium, Physical Review Letters 120, 150504 (2018), publisher: American Physical Society.

[5] H. Zhang, S. Chakram, T. Roy, N. Earnest, Y. Lu, Z. Huang, D. Weiss, J. Koch, and D. I. Schuster, Universal fast flux control of a coherent, low-frequency qubit, Physical Review X 11, 011010 (2021), arXiv:2002.10653 [cond-mat, physics:quant-ph].

[6] L. Ding, M. Hays, Y. Sung, B. Kannan, J. An, A. Di Paolo, A. H. Karamlou, T. M. Hazard, K. Azar, D. K. Kim, B. M. Niedzielski, A. Melville, M. E. Schwartz, J. L. Yoder, T. P. Orlando, S. Gustavsson, J. A. Grover, K. Serniak, and W. D. Oliver, High-Fidelity, Frequency-Flexible Two-Qubit Fluxonium Gates with a Transmon Coupler, Physical Review X 13, 031035 (2023), publisher: American Physical Society.

[7] H. Zhang, C. Ding, D. Weiss, Z. Huang, Y. Ma, C. Guinn, S. Sussman, S. P. Chitta, D. Chen, A. A. Houck, J. Koch, and D. I. Schuster, Tunable Inductive Coupler for High-Fidelity Gates Between Fluxonium Qubits, PRX Quantum 5, 020326 (2024), publisher: American Physical Society.

[8] K. N. Nesterov, C. Wang, V. E. Manucharyan, and M. G. Vavilov, cnot Gates for Fluxonium Qubits via Selective Darkening of Transitions, Physical Review Applied 18, 034063 (2022), publisher: American Physical Society.

[9] K. N. Nesterov, Q. Ficheux, V. E. Manucharyan, and M. G. Vavilov, Proposal for Entangling Gates on Fluxonium Qubits via a Two-Photon Transition, PRX Quantum 2, 020345 (2021), publisher: American Physical Society.

[10] E. Dogan, D. Rosenstock, L. Le Guevel, H. Xiong, R. A. Mencia, A. Somoroff, K. N. Nesterov, M. G. Vavilov, V. E. Manucharyan, and C. Wang, Two-Fluxonium Cross-Resonance Gate, Physical Review Applied 20, 024011 (2023), publisher: American Physical Society.

[11] E. L. Rosenfeld, C. T. Hann, D. I. Schuster, M. H. Matheny, and A. A. Clerk, Designing high-fidelity two-qubit gates between fluxonium qubits, arXiv preprint arXiv:2403.07242 (2024).

[12] PRX Quantum 3, 037001 (2022) - Blueprint for a High-Performance Fluxonium Quantum Processor (2022).

[13] N. A. Masluk, I. M. Pop, A. Kamal, Z. K. Minev, and M. H. Devoret, Microwave Characterization of Josephson Junction Arrays: Implementing a Low Loss Superinductance, Physical Review Letters 109, 137002 (2012), publisher: American Physical Society.

[14] F. Wang, K. Lu, H. Zhan, L. Ma, F. Wu, H. Sun, H. Deng, Y. Bai, F. Bao, X. Chang, et al., Achieving millisecond coherence fluxonium through overlap josephson junctions, arXiv preprint arXiv:2405.05481 (2024).

[15] D. G. Ferguson, A. A. Houck, and J. Koch, Symmetries and collective excitations in large superconducting circuits, Physical Review X 3, 011003 (2013).

[16] A. Blais, A. L. Grimsmo, S. M. Girvin, and A. Wallraff, Circuit quantum electrodynamics, Reviews of Modern Physics 93, 025005 (2021).

[17] R. Shillito, A. Petrescu, J. Cohen, J. Beall, M. Hauru, M. Ganahl, A. G. Lewis, G. Vidal, and A. Blais, Dynamics of transmon ionization, Physical Review Applied 18, 034031 (2022).

[18] X. Xiao, J. Venkatraman, R. G. Cortiñas, S. Chowdhury, and M. H. Devoret, A diagrammatic method to compute the effective hamiltonian of driven nonlinear oscillators, arXiv preprint arXiv:2304.13656 (2023).

[19] M. Khezri, A. Opremcak, Z. Chen, K. C. Miao, M. McEwen, A. Bengtsson, T. White, O. Naaman, D. Sank, A. N. Korotkov, et al., Measurement-induced state transitions in a superconducting qubit: Within the rotating-wave approximation, Physical Review Applied 20, 054008 (2023).

[20] J. Cohen, A. Petrescu, R. Shillito, and A. Blais, Reminiscence of classical chaos in driven transmons, PRX Quantum 4, 020312 (2023).

[21] M. F. Dumas, B. Groleau-Paré, A. McDonald, M. H. Muñoz-Arias, C. Lledó, B. D'Anjou, and A. Blais, Unified picture of measurement-induced ionization in the transmon, arXiv preprint arXiv:2402.06615 (2024).

[22] D. Sank, Z. Chen, M. Khezri, J. Kelly, R. Barends, B. Campbell, Y. Chen, B. Chiaro, A. Dunsworth, A. Fowler, et al., Measurement-induced state transitions in a superconducting qubit: Beyond the rotating wave approximation, Physical review letters 117, 190503 (2016).

[23] K. N. Nesterov and I. V. Pechenezhskiy, Measurement-induced state transitions in dispersive qubit readout schemes, arXiv preprint arXiv:2402.07360 (2024).

[24] L. B. Nguyen, Y.-H. Lin, A. Somoroff, R. Mencia, N. Grabon, and V. E. Manucharyan, High-coherence fluxonium qubit, Physical Review X **9**, 041041 (2019).

[25] V. E. Manucharyan, J. Koch, L. I. Glazman, and M. H. Devoret, Fluxonium: Single cooper-pair circuit free of charge offsets, Science **326**, 113 (2009).

[26] G. Viola and G. Catelani, Collective modes in the fluxonium qubit, Physical Review B **92**, 224511 (2015).

[27] D. Gusenkova, M. Spiecker, R. Gebauer, M. Willsch, D. Willsch, F. Valenti, N. Karcher, L. Grünhaupt, I. Takmakov, P. Winkel, *et al.*, Quantum nondemolition dispersive readout of a superconducting artificial atom using large photon numbers, Physical Review Applied **15**, 064030 (2021).

[28] In fact, the first four even parasitic modes with coupling strengths within a factor of 10 of $g_{\phi r}$. See Fig. 13 in App. B.

[29] T. N. Ikeda, S. Tanaka, and Y. Kayanuma, Floquet-landau-zener interferometry: Usefulness of the floquet theory in pulse-laser-driven systems, Physical Review Research **4**, 033075 (2022).

[30] We show that our results hold when simulated with 30 levels in the qubit mode and 10 levels in the parasitic mode.

[31] A relatively high-frequency choice, to reduce thermal, photon shot-noise induced dephasing in the qubit compared to lower-frequency bands.

[32] G. Zhu, D. G. Ferguson, V. E. Manucharyan, and J. Koch, Circuit QED with fluxonium qubits: Theory of the dispersive regime, Physical Review B **87**, 024510 (2013), publisher: American Physical Society.

[33] N. A. Masluk, *Reducing the losses of the fluxonium artificial atom* (Yale University, 2013).

[34] A. G. Fowler, M. Mariantoni, J. M. Martinis, and A. N. Cleland, Surface codes: Towards practical large-scale quantum computation, Physical Review A—Atomic, Molecular, and Optical Physics **86**, 032324 (2012).

[35] L. Ding, M. Hays, Y. Sung, B. Kannan, J. An, A. Di Paolo, A. H. Karamlou, T. M. Hazard, K. Azar, D. K. Kim, *et al.*, High-fidelity, frequency-flexible two-qubit fluxonium gates with a transmon coupler, Physical Review X **13**, 031035 (2023).

[36] S. Hazra, W. Dai, T. Connolly, P. Kurilovich, Z. Wang, L. Frunzio, and M. Devoret, Benchmarking the readout of a superconducting qubit for repeated measurements, arXiv preprint arXiv:2407.10934 (2024).

[37] Z. Huang, P. S. Mundada, A. Gyenis, D. I. Schuster, A. A. Houck, and J. Koch, Engineering dynamical sweet spots to protect qubits from $1/f$ noise, Phys. Rev. Appl. **15**, 034065 (2021).

[38] M. D. Reed, L. DiCarlo, B. R. Johnson, L. Sun, D. I. Schuster, L. Frunzio, and R. J. Schoelkopf, High-Fidelity Readout in Circuit Quantum Electrodynamics Using the Jaynes-Cummings Nonlinearity, Physical Review Letters **105**, 173601 (2010), publisher: American Physical Society.

[39] M. H. Muñoz-Arias, C. Lledó, and A. Blais, Qubit readout enabled by qubit cloaking, Physical Review Applied **20**, 054013 (2023), publisher: American Physical Society.

[40] N. Didier, J. Bourassa, and A. Blais, Fast Quantum Nondemolition Readout by Parametric Modulation of Longitudinal Qubit-Oscillator Interaction, Physical Review Letters **115**, 203601 (2015), publisher: American Physical Society.

[41] G. Catelani, R. J. Schoelkopf, M. H. Devoret, and L. I. Glazman, Relaxation and frequency shifts induced by quasiparticles in superconducting qubits, Physical Review B **84**, 064517 (2011).

[42] J. Koch, V. Manucharyan, M. Devoret, and L. Glazman, Charging effects in the inductively shunted josephson junction, Physical review letters **103**, 217004 (2009).

[43] Alternatively, for the coupling strengths with readout, we multiply with the constant factor of $\frac{1}{2\pi}\omega_r\sqrt{\frac{\pi Z}{R_K}} \approx 1$ in GHz for (eV/h), where $R_k = h/e^2 = 25.8K\Omega$, $Z = 50*4/\pi\Omega$, $\omega_r \approx 10$GHz. Thus, $eVZPF/h = 0.14$ which can be checked against $n_{ZPF,r}$ quoted for chip 2(A&B) as follows. $n = Q/2e = CV/2e = (eV/h)/\omega_r * Z_r * 2e^2/h = 0.14/(2\omega_r * Z_r/R_k) = 2.84$.

[44] J. Gambetta, A. Blais, D. I. Schuster, A. Wallraff, L. Frunzio, J. Majer, M. H. Devoret, S. M. Girvin, and R. J. Schoelkopf, Qubit-photon interactions in a cavity: Measurement-induced dephasing and number splitting, Physical Review A **74**, 042318 (2006).

[45] A. Clerk and D. W. Utami, Using a qubit to measure photon-number statistics of a driven thermal oscillator, Physical Review A—Atomic, Molecular, and Optical Physics **75**, 042302 (2007).